Highlights

- The most popular BPS tools, namely TRNSYS, EnergyPlus and IDA ICE, are compared
- Two different small-scale solar test boxes were employed for the accuracy assessment
- The comparison was developed both in the presence and absence of a PCM module on the floor
- Warm, intermediate and cold periods were considered for the comparison
- All tools are highly accurate in the absence of PCM, while IDA ICE use is recommendable in the presence of PCM

EnergyPlus, IDA ICE and TRNSYS predictive simulation accuracy for building thermal behaviour evaluation by using an experimental campaign in solar test boxes with and without a PCM module

Domenico Mazzeo[a,b], Nicoletta Matera[b], Cristina Cornaro[c], Giuseppe Oliveti[b], Piercarlo Romagnoni[a], Livio De Santoli[d]

[a]*University IUAV of Venice, Department of Design and Planning in Complex Environments*
[b]*University of Calabria, Department of Mechanical, Energy and Management Engineering*
[c]*University of Rome "Tor Vergata", Department of Enterprise Engineering*
[d]*University of Rome "La Sapienza", Department of Astronautics, Electrical and Energy Engineering*

Abstract

For the design of new buildings or buildings undergoing major renovations, the use of building performance simulation (BPS) tools is a key instrument to sizing the envelope or to select the best solution to be integrated. Nowadays, many BPS tools are available and are used by researchers and designers, each of which was independently validated, by considering different operating conditions, and rarely were directly compared in the same conditions. The objective of this work is to evaluate the prediction accuracy of the most popular BPS tools, namely TRNSYS, EnergyPlus and IDA ICE, by means of a comparison of the simulated results and the experimental measurements detected under real operating conditions. For this issue, two different small-scale solar test boxes (STBs) with one glazed wall exposed to the outdoor environment of Rome were employed for the experimental investigation. The envelope of the reference STB is insulated and made by conventional materials. In the other case, the STB floor is equipped also with a commercial phase change material (PCM) panel. Both STBs were equipped with a data acquisition system to detect the internal air temperature, the glass external and internal surface temperature and, for the PCM-based STB, also the PCM floor internal surface temperature.

A wide description and comparison of the mathematical models used by the three BPS tools are provided, followed by a geometric, weather data, technical and heat transfer parameters alignment was developed to put all the tools in the same conditions. Three different experimental campaign periods were considered and used for the evaluation of each BPS tool accuracy.

Some common accuracy indices were used for the comparison, such as the R2, RMSE and normalized RMSE, and an overall accuracy index that summarizes the previous ones in the different experimental campaign periods. The results have shown have highlighted the most accurate mathematical models for the prediction of the dynamic thermal behaviour of the STB in the absence and presence of a PCM. In the absence of PCM in the STB, all the three tools are comparable providing high overall accuracy index in all periods with a rank variable as a function of the period owing to the different treatment of the solar radiation modelling. In the presence of PCM in the STB, IDA ICE leads to the highest overall accuracy index in all periods. Unlike to IDA ICE, TRNSYS and EnergyPlus do not take into account the PCM hysteresis phenomenon. Instead, TRNSYS model provides the worst accuracy since it neglects both hysteresis and phase change temperature range, that is instead implemented both in IDA ICE and EnergyPlus. However, TRNSYS predictions can be retained acceptable for a preliminary evaluation since only low data and very low computational cost is required.

Keywords: Building performance simulation; TRNSYS; EnergyPlus; IDA ICE; Experimental campaign; Accuracy

1. Introduction

The buildings sector is the largest energy-consuming sector, accounting for over one-third of final energy consumption globally and an equally important source of carbon dioxide (CO_2) emissions [1]. The energy

intensity per square meter of the global buildings sector needs to improve on average by 30% by 2030, compared to 2015, to be on track to meet global climate ambitions set out in the Paris Agreement [2]. Rapid deployment of energy-efficient and low-carbon solutions and construction for buildings can help put the world on a sustainable trajectory. Some of the technologies needed to transform the buildings sector are already commercially available and cost-effective, with payback periods of less than five years. The potential of these technologies is normally estimated by using Building Performance Simulation (BPS) tools, which has become a key instrument in the evaluation of the building energy demand and thermal comfort. As regards new buildings, they allow a user to design properly the envelope, while in the case of buildings undergoing major renovation permit to identify the most properly interventions to reduce energy needs and improve the indoor thermal comfort. Over the past 50 years, according to the literature review, many dynamic simulation tools were developed [3, 4]. The main differences between the BPS tools are represented by the mathematical models employed to predict the conductive, convective and longwave and shortwave radiative heat transfer between the external envelope and the indoor and outdoor environments [10-12]. In addition to having sophisticated models, researchers usually choose which software to use to perform thermal dynamic simulations of buildings as a function of flexibility in the extension of the standard library, execution speed, difficulty of use and possibility of access to the source code. The BPS tools can be classified as general-purpose or special-purpose simulation tools. By means of the first typology of tools, the users can define proper mathematical models making them more flexible with the disadvantage of difficulty of use and low execution speed. Instead, in the second typology of tools, different predefined standard simulation problems are available and permit to obtain a high execution speed, with the disadvantage of lower flexibility in the simulation of non-standard problems. Consequently, the two typologies differ mainly for source code access and modification mode, and simulation control capability.

By considering the requirements for accurate, flexible, easy and high execution speed dynamic simulations, among the tools available, TRaNsient SYstem Simulation 17 (TRNSYS) [5], EnergyPlus 8.6 [6] and IDA Indoor Climate and Energy (ICE) [7] have nowadays become the most widespread.

TRNSYS and IDAICE fall into the first typology, while EnergyPlus in the second one. TRNSYS, developed at the Solar Energy Laboratory of the University of Wisconsin-Madison, is a flexible transient system simulation program for complex systems with a modular structure, characterised by the division of a problem into a series of smaller subproblems contained in specific components or Types. In addition, new models can be compiled into new components and introduced in the TRNSYS library. TRNbuild [8] is an interface for the geometric, thermal and optical definition of a specific building. IDA ICE is a flexible whole-building performance simulation tool, developed at Department of Building Sciences (Stockholm), which works with symbolic equations instead of variable assignments, and therefore it is relatively easy to extend the existing modelling functionality. EnergyPlus, developed by the U.S. Department of Energy, is a whole building energy simulation program based on a modular structure that has shown a continuous enhancement in the possibility of adding validated new models. DesignBuilder [9] provides an easy-to-use interface to develop building designs from concept through to completion.

The selected tools have been extensively used for this purpose and were individually validated. However, these validations were obtained for different climatic conditions and buildings. For this reason, it is not possible to make a direct comparison of their prediction with the current findings and knowledge. In addition, in the last years, new materials were proposed to improve the thermal response of building envelope in the winter and summer period, such as phase change materials (PCMs), green roofs and facades, cool materials, vacuum super insulation materials and so on. For this issue, the abovementioned tools have integrated into own library new simulation subroutines able to predict the thermal response of buildings containing these innovative materials. In particular, passive cooling and heating by means of PCM application in walls off er high potential to improve the building dynamic and energy performance [13] and have attracted the attention of many researchers, for the development of mathematical models [14] and companies for the production of PCM-based products. For researchers and designers, the BPS tools are

fundamental to appropriately characterize and integrate PCM into the building envelope. The simulation subroutines developed by the abovementioned tools employ different mathematical models for PCM thermal behaviour prediction and, consequently, it is necessary to evaluate which approach is the most appropriate. In several studies, these subroutines were validated and extensively used to evaluate the behaviour of PCM in buildings. In particular, IDA ICE PCM tool was validated in previous work by employing the same STB used in this research [15, 16]. Instead, Type 1270 of TRNSYS was validated by Jayalath et al. [17] and Panayiotou et al. [18], while EnergyPlus PCM tool by Tabares-Velasco et al. [19]. All tools have shown a good agreement with the experimental data despite the different assumptions. The previous researches were conducted considering real operating conditions in an outdoor environment or thermally controlled test boxes. Consequently, nonetheless the large employment of BPS tools, there is a gap in the knowledge of the result accuracy provided by the different models in the same conditions.

In the literature, to the best knowledge of the author of this article, it is not present a direct comparison between the different BPS tools and experimental data detected both in the absence and in the presence of PCM.

For this purpose, the research aims to evaluate the effect produced by the different building simulation models implemented in the BPS tools considered on the prediction accuracy. Two solar test boxes with and without PCM were used for the experimental campaign developed in a warm, intermediate and cold period. First of all, an alignment between the geometric, climatic data, technical parameters were made in TRNSYS, EnergyPlus and IDA ICE, to attribute the deviations of the results only to the model accuracy. To evaluate the BPS accuracies, for the different experimental campaign periods and measured STB temperatures, a group of some of the most common metrics, such as the coefficient of determination (R^2), root mean square error (RMSE), and normalized RMSE, were used. Finally, both in the absence and in the presence of PCM, a BPS ranking is provided based on the use of a synthetic overall index independent of the period considered.

2. Methodology

In this Section, the solar test boxes designed to make a comparison between the predictions of the three dynamic simulation tools considered, namely TRNSYS, EnergyPlus, and IDA ICE, are presented. For this issue, the geometrical and thermophysical properties of the solar test boxes in the absence and presence of PCM are presented in Section 2.1. A list of data acquisition devices in the indoor and outdoor environment is also reported. Moreover, the outdoor climate data measurements in the selected periods are described in Section 2.2. Subsequently, a direct comparison between the different mathematical models used by the three tools for the thermal exchange prediction through the STBs is reported in Section 2.3.

Finally, the accuracy indices used to identify the most accurate tool are defined in Section 2.4. Figure 1 reports a schematic view of this research content.

Figure 1 – Schematic view of the experimental and simulation campaign.

The figure shows, both for the reference and PCM-based STB, the selected periods in which the three tools are compared each other with the experimental results, the thermal measurements and the accuracy indices employed for the comparison

2.1 Experimental equipment

Figure 2 shows the reference Solar Test Box STB employed for the experimental comparison of the three BPS tools, built at the ESTER laboratory of the University of Rome “Tor Vergata”. An identical STB was also considered with a PCM layer placed on the internal surface of the floor.

Figure 2 – Real 3D view, and 2D section planes and views of the PCM-based solar test box.

The two STBs are raised of 75 cm above the basement by wooden trestles. They have dimensions 1.00 × 0.60 × 0.55 m externally and 0.872 × 0.424 × 0.374 m internally, starting from which the wall thicknesses can be deducted as shown in Figure 2. All the external walls consist, from the external side to the internal one, of a plywood layer of 0.008 m and an insulation layer of 0.08 m. Only the southern opaque wall is different since at the beginning the window system was greater [15] and successively was covered by a plywood panel to obtain a reduced window area. This allowed us to control the solar heat transfer through the window and incident on the floor to guarantee the reaching of the phase change temperature on the floor triggering the phase change process. Therefore, in this circumstance, the southern wall consists of a boundary part with the same stratigraphy of the other orientations and another part, devoid of insulation, composed by plywood and window system from the external side to the internal one, with a thermal transmittance of 1.345 W/m^2 K.
Being the external wall stratigraphies highly insulated with a thermal transmittance of 0.280 W/m^2 K, the main contribution on the indoor thermal zone balance is represented by the solar radiation penetrating through the window wall. The window system is constituted by a clear double glazed pane, 4-12-4 mm, with a thermal transmittance of 2.712 W/m^2K, solar heat gain coefficient of 0.76 and a normal solar transmission coefficient of 0.70. The dimensions 0.20x0.30 m of the southern exposed glassed surface were made to obtain STB indoor temperature around the phase change temperatures of the PCM such as to activate the latent storage phenomenon and to avoid damages to the PCM panel owing to high temperatures.
The thermophysical (density r, thermal conductivity λ and specific heat capacity c_p) properties and longwave and shortwave optical properties (emissivity ε and absorptivity α) of the materials are resumed in Table 1.

Table 1: Thermophysical and optical properties of the wall layers of the solar test box.

The PCM panel considered is the SP21E provided by the RUBITHERM, Technologies GmbH, and it has dimensions of 0.45x0.30x0.015 m [20]. The PCM thermophysical properties in the liquid and solid phases are listed in Table 2.

Table 2: Thermophysical properties of the PCM layer.

The panel is coated with an aluminium casing treated on the surface to make it anti-corrosive and contains 2 kg of microencapsulated inorganic PCM. To take into account the real PCM quantity of 2 kg inside the aluminium case, an equivalent thickness of 0.0102 m was calculated, by excluding capsule and air gaps volume. The optical properties of the aluminium are emissivity of 0.60 and absorptivity of 0.40 [21]. Finally, the specific heat capacity and the enthalpy curves as a function of the temperature, both in the heating fusion process and cooling solidification process are shown in Figure 3.

Figure 3 – Enthalpy and specific heat capacity as a function of the temperature for a heating and cooling process.

The PCM presents a moderate hysteresis since the fusion and solidification enthalpy curve are not overlapped, with fusion and solidification peak temperatures of respectively 20 °C and 22 °C. The overall latent energy stored during a complete solidification/fusion process is 129 kJ/kg.
A value of 0.5 vol/h is employed to summarize the external air infiltration flow rate taking into account the sealing level of the test box [15].
The use of this STB with reduced dimensions and internal volume permits to amplify the effects produced by the PCM module on the thermal behaviour into the STB.

2.2 *Description of the short-term monitoring campaigns selected*

Each STB is equipped by a measurement system and the ESTER lab owns a weather station located in proximity to the STBs. Table 3 lists the thermal quantities measured, the devices employed and the accuracy.

Table 3 – Measurement devices in the solar test box and outdoor environment.

Further details on the measurement and sensors location can be found within previous works [15, 16].
Three different short-term monitoring periods were considered, characterized by a high range of variability of the ratio of horizontal global solar radiation and the corresponding extraterrestrial one, namely the daily clearness index, between of 0.09 and 0.68:

- the first experimental campaign ranges between 26th September at 11:00 to the 30th of September at 11:00 with a daily clearness index between 0.55 and 0.68;
- the second experimental campaign ranges between 21st November at 11:00 to the 24th of November at 8:00 with a daily clearness index between 0.38 and 0.57;
- the third experimental campaign ranges between 5th December at 14:00 to the 9th of December at 9:00 with a daily clearness index between 0.09 and 0.63.

In this way, different solar irradiance conditions are considered to make the comparison more comprehensive. Figure 4 reports all the outdoor climate data in the selected periods.

Figure 4 – Weather conditions in the three periods of the experimental campaign.

The external air temperature is moderately different in the three periods considered and it ranges between 14.7 °C and 26.0 °C in the first experimental campaign, 11.5 °C and 21.6 °C in the second experimental campaign, and 2.8 °C and 17.5 °C in the third experimental campaign.
The high range of variability of the clearness index permitted to consider different climate conditions in the analysis developed. Instead, a direct comparison between the equivalent external air temperature [22] and the fusion and solidification peak temperatures, as shown in Figure 5, has permitted to preliminarily identify different PCM behaviours.

Figure 5 – Equivalent external air temperature in the three experimental campaigns compared with the melting and solidification peak temperatures.

The figure highlights that the phase change phenomenon is activated in all days of the three periods, except in the first day of December, when the PCM stays always in the solid phase, being the equivalent external air temperature always higher than the melting peak temperature. In the other days, different amplitudes of the thermal waves in the heating and cooling processes are observed. For this reason, in the different days of the three periods, the PCM layer is entirely or partially melted or solidified as a function of the daily thermal excursion available.

2.3 *Solar test box heat transfer models*

The described STB was geometrically and thermally modelled within three popular building performance simulation tools, namely TRaNsient SYstem Simulation (TRNSYS) 17, EnergyPlus 8.6 and IDA Indoor Climate and Energy (ICE) 4.8. These tools employ different mathematical models, more or less sophisticated, to describe the heat transfer between the building envelope and the outdoor and indoor environment according to the three mechanisms of conduction, convection, and radiation [10-12]. Hereafter, all the mathematical models used by the three tools are described and compared.
The thermal balance of the STB thermal zone devoid of the HVAC system can be expressed by the Eq. (1).

$$\boldsymbol{Q_{STB} = Q_{inf} + Q_{s,i} = C_a \frac{dT}{dt}} \quad (\mathbf{1})$$

This equation quantifies the overall convective thermal power Q_{STB} that is transferred by the air node by determining the change of internal energy of zone. In Eq. (1), C is the heat capacity of the air, Q_{inf} is the infiltration heat gain (air flow from outside only) and $Q_{s,i}$ is the convective gain from internal surfaces. For the STB, $Q_{s,i}$ is the sum of the convective gains coming from the opaque surface differently oriented and from the glass surface exposed to South $Q_{g,i}$:

$$\boldsymbol{Q_{s,i} = Q_s + Q_w + Q_n + Q_e + Q_f + Q_r + Q_{g,i}} \quad (\mathbf{2})$$

For the reference STB, the floor convective gain Q_f is the product between the heat flux q_f and the relative surface area S_f. For the PCM-based STB, the floor convective gain Q_f is the sum of that coming from the PCM surface $q_{PCM}S_{PCM}$ and that coming from the surface devoid of PCM q'_f (S_f - S_{PCM}).
To determine the generic convective heat flux q, the heat conduction through the wall is solved by imposing the heat balance equations on the external and on the internal surfaces.

2.3.1 Heat balance equation on the internal surface

The heat balance involving the inside surfaces of the STB can be written as follows:

$$q_{sol,i} + q_{lw,i} + q_{cv,i} + q_{cd,i} = 0 \quad (3)$$

where, $q_{sol,i}$ is the transmitted solar radiation through the windowed walls absorbed by the internal surface, $q_{lw,i}$ is the net longwave radiant exchange heat flux between zone surfaces, $q_{cv,i}$ is the convective heat flux to zone air, and $q_{cd,i}$ is the conduction heat flux through the wall at the interface with the zone air.

2.3.1.1 Convective thermal exchange

The internal convective heat flux is calculated as a function of the internal surface convective heat transfer coefficient $h_{c,i}$:

$$q_{cv,i} = h_{cv,i}(T_{s,i} - T_{a,i}) \quad (4)$$

The three BPS tools mainly differ on the basis of the options and flexibility offered to set the internal surface convective heat transfer coefficient.
For example, TRNSYS permits to set the internal convective heat transfer coefficient as a constant, input or scheduled value. The input value permits to implement any equation model available in the scientific literature. Alternatively, an internal calculation model can be active which consists of using the following equation:

$$h_{cv,i} = K(T_{s,i} - T_{a,i})^Y \quad (5)$$

where, K and Y depend on the surface inclination and heat flux direction.
In an analogous manner to this latter TRNSYS option, IDA ICE calculates the internal surface convective heat transfer coefficient as a function of the temperature difference between the air and the surface and the slope of the surface. Unlike to IDA ICE and TRNSYS, the adaptive convection algorithm of EnergyPlus provides many different models based on correlations for natural, mixed, and forced convection, depending on the surface orientations, room airflow conditions, and heat flux direction. The adaptive convection

algorithm implemented in EnergyPlus for the inside face has a total of 45 different categories for surfaces and 29 different options.

2.3.1.2 Longwave radiative thermal exchange

In all the BPS tools, a cavity composed of grey surfaces is considered with surface emissivities and reflectivity independent of wavelength and direction.

TRNSYS detailed mode employs the Gebhart method, which by means a so-called Gebhart factor evaluates the radiation absorbed by a surface coming by another generic surface, by considering all the possible paths and also the multiple reflections. The net absorbed longwave radiation in a matrix form is calculated as follows:

$$Q_{lw,i} = \left(I - G_{lw}^{T}\right)A\varepsilon\sigma\widehat{T}^{4} = \{I - [(I - F\rho_{lw})^{-1}F\varepsilon_{lw}]^{T}\}A\varepsilon\sigma\widehat{T}^{4} \quad (6)$$

where, $Q_{lw,i}$ is net absorbed longwave radiation vector, G_{lw} the Gebhart matrix, which is a function of the emissivity ε, reflectivity ρ and view factor F matrices, A the diagonal matrix of surface area, and T the surface temperature vector.

EnergyPlus includes the Hottel method based on the calculation of the "ScriptF" matrix. This matrix contains the exchange coefficients that describe the thermal exchange between all the surfaces following all exchange paths and considering all reflections, absorptions, and re-emissions. The generic net longwave radiation exchange between the surface i and surface j is calculated with the following equation:

$$Q_{lw,ij} = A_i F_{ij}\left(T_i^4 - T_j^4\right) \quad (7)$$

where F_{ij} is the ScriptF coefficient between surfaces i e j.

Analogously, in IDA ICE a net longwave absorption matrix $psi_{lw,i}$, containing all cavity geometrical and optical properties, is used to calculate the net absorbed longwave radiation $Q_{lw,i}$, obtained as a difference between the irradiance onto one surface and the radiosity:

$$Q_{lw,i} = psi_{lw,i}W_b \quad (8)$$

Where, W_b is the black body emissive power.

2.3.1.3 Shortwave diffuse radiative thermal exchange

In the detailed mode of TRNSYS, a so-called solar Gebhart matrix G_{difsol} is considered in adherence at the treatment of the longwave radiation. By considering all direct and multi reflecting paths, this matrix allows evaluation of the fraction of transmitted solar radiation through a surface that reaches another surface and it is not reflected.

The absorbed diffuse solar radiation in the cavity Q_{difsol} is:

$$Q_{difsol} = -G_{difsol}{}^{T}AI_{difsol} = -[(I - F\rho_{sw})^{-1}F(I - \rho_{sw})]^{T}A_g I_{difsol} \quad (9)$$

where, Q_{dif} is net absorbed shortwave radiation vector, G_{difsol} the solar Gebhart matrix, which is a function of the reflectivity ρ and view factor matrices F, A the diagonal matrix of surface area, and I_{dif} the diffuse solar radiation transmitted through the window surface.

Also IDA ICE considers a net shortwave net absorption matrix psi_{sw} to calculate the net short-wave radiation absorbed Q_{difsol}:

$$Q_{difsol} = psi_{sw}I_{difsol} \quad (10)$$

EnergyPlus is the least accurate since distributes the diffuse solar radiation through the window surface A_g on the internal walls in proportion to the product $\alpha_i A_i$, with α_i absorptivity and A_i area of the i-th surface according to the following equation:

$$Q_{difsol,i} = \frac{\alpha_i A_i}{\sum \alpha_i A_i} A_g I_{difsol} \quad (11)$$

2.3.1.4 Shortwave direct radiative thermal exchange

TRNSYS allows the treatment of the shortwave direct radiation in a sophisticated manner since employs a detailed mode, which is based on a primary distribution of the direct solar radiation through the window wall by means of the insolation matrices calculate by the auxiliary program TRNSHED. These matrices contain the beam sunlit fractions for each cavity internal surface for all the patches of the celestial hemisphere. In this way, at each time step, the matrix row is selected as a function of the actual sun position. Once the primary direct solar radiation was distributed on the internal surfaces, the reflected part is considered diffuse. In a similar way to TRNSYS, EnergyPlus assumes that all transmitted beam solar can befall on each surface of the cavity, including floor, walls, and windows, by projecting the sun's rays through the exterior window. For this issue, by means of shadowing routines, it calculates an overlap area, irradiated area by the beam solar radiation of the internal surfaces projected on the exterior window, as a function of the sun position, the geometry of the window, the geometry of the interior surfaces, and the location of the window with respect to the interior surfaces. For the purposes of the surface heat balance calculation, any beam solar radiation absorbed by a surface is assumed to be uniformly distributed over the surface. Finally, IDA ICE presents the least accurate model since the direct solar radiation is considered as diffuse after the crossing of the window.

2.3.2 Heat balance equation on the external surface

The heat balance involving the outside surfaces of the STB can be written as follows:

$$q_{sol,e} + q_{lw,e} + q_{cv,e} - q_{cd,e} = 0 \quad (12)$$

where $q_{sol,e}$ is the direct and diffuse solar radiation absorbed by the external surface, $q_{lw,e}$ is the net longwave radiation heat flux exchange with the surroundings, $q_{cv,e}$ is the convective heat flux to the external air, and $q_{cd,e}$ is the conduction heat flux through the wall at the interface with the outdoor environment.

2.3.2.1 Convective thermal exchange

The external convective heat flux is calculated as a function of the external surface convective heat transfer coefficient $h_{cv,e}$:

$$q_{cv,e} = h_{cv,e}(T_{a,e} - T_{s,e}) \quad (13)$$

The three BPS tools mainly differ on the basis of the options and flexibility offered to set the external surface convective heat transfer coefficient

For example, IDA ICE is the least flexible since $h_{cv,e}$ is determined by employing the following correlation:

$$h_{cv,e} = 5.678\left[a + b\left(\frac{V}{0.3048}\right)^c\right] \quad (14)$$

where, the local wind velocity V at the leeward side is calculated as a function of the free-stream wind speed V_f :

$$V = 0.3 + 0.05V_f \quad (15)$$

and a, b and c are constant coefficients:

$$\begin{cases} a = 1.09, b = 0.23, c = 1 & V < 4.88\,\frac{m}{s} \\ a = 0, b = 0.53, c = 0.78 & V \geq 4.88\,\frac{m}{s} \end{cases} \quad (16)$$

Unlike to IDA ICE, EnegyPlus and TRNSYS contain a width list of models and options of different complexity and approximation for the calculation of $h_{c,e}$.
In EnergyPlus, the options included are:

- SimpleCombined: uses surface roughness and local surface wind speed;
- Detailed, BLAST, and TARP: sum of a forced and a natural component, calculated respectively by taking into account the surface roughness and local wind speed, and the difference between the external surface and air temperatures and inclination of the wall;
- MoWiTT: applicable to very smooth and vertical surfaces, e.g. window glass, and depends on the wind speed at the height above ground and difference between the external surface and air temperatures, and distinguish between windward and leeward surface placement;
- DOE-2: is a combination of the MoWiTT and BLAST Detailed convection models;
- AdaptiveConvectionAlgorithm: identify four different surface categories dependent on wind and heat flow directions; also in this case, the convective heat transfer coefficient is split into two separate models for forced and natural convection.

In TRNSYS, the external convective heat transfer coefficient can be set as a constant, input or scheduled value. The input value permits to implement any equation model available in the scientific literature. Alternatively, an internal calculation model can be active which consists of using the following equation:

$$h_{cv,e} = K(T_{s,e} - T_{a,e})^{Y} \quad (17)$$

where, K and Y depend on the surface inclination and heat flux direction.

2.3.2.2 Shortwave radiative thermal exchange

All three tools use the following equation to evaluate the absorbed solar radiation by the external surface.

$$q_{sol,e} = \alpha_e(G_b + G_d + G_r) \quad (18)$$

Where, α_e is the external surface absorptivity, G_b, G_d, and G_r are the beam, diffuse and reflected solar radiation on the inclined surface.

2.3.2.3 Longwave radiative thermal exchange

The wall is considered as a grey body, while the ground, sky, and air are considered as black bodies.
In EnergyPlus, the net longwave radiative heat flux at the building exterior surface is schematized as the sum of components due to radiative exchange with the ground $q_{lw,gnd}$, sky $q_{lw,sky}$, and air $q_{lw,air}$:

$$\begin{aligned} q_{lw,e} &= q_{lw,grd} + q_{lw,sky} + q_{lw,air} \\ &= \varepsilon_{s,e}\sigma F_{grd}\left(T^4_{grd} - T^4_{s,e}\right) + \varepsilon_{s,e}\sigma F_{sky}\left(T^4_{sky} - T^4_{s,e}\right) + \varepsilon_{s,e}\sigma F_{air}\left(T^4_{air} - T^4_{s,e}\right) \end{aligned} \quad (19)$$

In Eq. (5), F are the view factors, $\varepsilon_{s,e}$ emissivity of the external surface and σ Stefan-Boltzmann constant.
The exchange with air permits to take into account the effect of the longwave radiation absorption owing to the water vapour and other compounds such as CO_2 in the atmosphere. The sky view factor is reduced and this reduction is attributed to the air view factor as a function of the surface inclination [23].

Instead, TRNSYS considers a fictive temperature of the surroundings T_{fsky}, calculated as the weighted mean, by the respective view factors, of the sky and ground temperatures T_{sky} and T_{grd}:

$$T_{fsky} = (1 - F_{sky})T_{grd} - F_{sky}T_{sky} \quad (20)$$

The net longwave radiative heat flux at the building exterior surface is computed by considering a sole component:

$$q_{lw,e} = \varepsilon_{s,e}\sigma(T^4{}_{fsky} - T^4{}_{s,e}) \quad (21)$$

Finally, in IDA ICE the net longwave radiation between the exterior surfaces and the ground and the sky is calculated by considering only the first two terms of Eq. (19).

2.3.3 Conductive in the opaque walls

The conductive heat transfer phenomenon in an opaque wall subject to the boundary conditions on the external and internal surface previously described is differently modelled and solved with different algorithms. TRNSYS employs a black box method based on the transfer function or response factor relationships defined from surface to surface. This method uses the historical time series of the surface temperature and heat flux values, until to *p* previous time instants, of which *p* values of the coefficients a_s, b_s, c_s and d_s are determined using the z-transfer function routines.

$$q_{cd,i} = \sum_{k=0}^{p_{b_s}} b^k{}_s T^k{}_{s,e} - \sum_{k=0}^{p_{c_s}} c^k{}_s T^k{}_{s,i} - \sum_{k=1}^{p_{d_s}} d^k{}_s q^k{}_{cd,i} \quad (22)$$

$$q_{cd,e} = \sum_{k=0}^{p_{a_s}} a^k{}_s T^k{}_{s,e} - \sum_{k=0}^{p_{b_s}} b^k{}_s T^k{}_{s,i} - \sum_{k=1}^{p_{d_s}} d^k{}_s q^k{}_{cd,e} \quad (23)$$

In EnergyPlus, the user can choose between two different approaches: the Conduction Transfer Function CTF method and the Conduction Finite Difference Solution Algorithm. The first method is analogous to that of TRNSYS and differs only for the method used for CTF calculation, namely the state space method. The second one was added to simulate materials with variable thermal conductivity and specific heat capacity with the temperature, and a semi-implicit Crank-Nicholson scheme and a fully implicit scheme can be chosen to solve the equation system. For an internal node, the fully implicit formulation is expressed by the following equation:

$$C_p r\Delta x \frac{T_j{}^{n+1} - T_j{}^n}{\Delta t} = \frac{1}{2}\left(k_{j,j+1}\frac{T_{j+1}{}^{n+1} - T_j{}^{n+1}}{\Delta x} + k_{j-1,j}\frac{T_{j-1}{}^{n+1} - T_j{}^{n+1}}{\Delta x} + k_{j,j+1}\frac{T_{j+1}{}^n - T_j{}^n}{\Delta x} + k_{j-1,j}\frac{T_{j-1}{}^n - T_j{}^n}{\Delta x}\right) \quad (24)$$

Finally, also IDA ICE uses a finite difference method, but with only three internal nodes, based on an RC network model with three capacitances to reduce the computational cost of the simulation. To choose the node position, an optimization subroutine is implemented to minimize the sum of the squares of the deviations obtained when the numerical solution is compared with the analytical solution to harmonic boundary conditions for different frequencies.

2.3.4 Optical and thermal transfer in the windowed walls

Both TRNSYS and EnergyPlus employ a detailed optical and thermal model of windows. In particular, a layer-by-layer approach is considered to determine the temperature of each glass pane that composes the

window system. These temperatures are calculated by considering the following optical and thermal phenomena:

- the direct and diffuse solar radiation transmitted, reflected and absorbed coming from the outdoor environment;
- the diffuse shortwave radiation coming from the indoor environment reflected by the walls;
- the convective, conductive and longwave radiative heat transfer between the individual panes and with the indoor and outdoor environment.

As regards the optical transfer, a link with WINDOW 4.1 program [24], created by Lawrence Berkeley Laboratory (USA), permits to develop, for windows with up to six panes, a detailed calculation of reflection between the individual panes and the absorption and transmission of each pane. This calculation is performed hemispherically for diffuse radiation and in steps of 10° incidence angle for direct solar radiation. In addition, WINDOW provides the optical spectral data in the entire visual and solar bands, the thermal properties of the gas fillings, the glazings conductivity and emissivity, and the thermal transmittance for different wind speeds and external air temperatures.

Also as regards the thermal transfer, TRNSYS and EnergyPlus employ an analogous approach. In particular, they consider separately the conduction, convection and longwave radiation between the individual glass panes. In both cases, pane temperatures are determined by means of an iterative procedure, to update the convective and radiative heat transfer coefficients, that is stopped when the change of pane temperatures is lower than a specified tolerance. In EnergyPlus, the window glass pane temperatures are determined by solving the heat balance equations on each glass face every time step. For a window with N glass layers, there are 2N faces and therefore a system of 2N equations to solve. The value of the inside face temperature T_{2N} permits to calculate Q_{gl} that participates in the Eq. (2).

In TRNSYS, once that the individual pane temperatures and all of the heat fluxes through the glazings are known, the overall absorbed shortwave radiation is calculated and successively distributed to the surface internal and external nodes. In this way, the window model allows determination of the heat fluxes of the two-node model, of which that internal one intervenes in the heat balance equation, Eq.(3), of the air node. The two nodes are correlated by means of the heat conduction equation, Eqs. (22) and (23), by considering the coefficients a_s, b_s, c_s and d_s equal to zero for k>0 and equal to the glass thermal transmittance U_g for k=0. The IDA ICE implements the simplified model for the window system that divides the solar radiation entering through a window into two parts: that directly transmitted and distributed as shortwave radiation to the zone; that first absorbed and then released to the zone as longwave radiation and convection. In particular, the total solar heat gain is calculated by considering the direct radiation reduced by a factor, which depends on the angle of incidence, and the diffuse radiation reduced by a constant hemispherical factor. Starting from this solar contribute and that coming from the indoor environment, the overall solar radiation absorbed in the window is calculated. Finally, the heat balance equations on the two outermost surfaces are solved.

In conclusion, both TRNSYS and IDA ICE aims to evaluate the overall solar radiation absorbed by the window system: in the first case in a detailed manner and in the second case in a simplified manner. Successively this absorbed solar radiation is split equally on the two boundary faces and the surface heat balance equations are solved. Instead, EnergyPlus considers the heat balance equation of each face of each glass pane and the solar radiation absorbed by each glass pane is equally divided on the two faces of the glass pane. EnergyPlus includes an alternate simplified model that reuses the layer-by-layer approach but converts an arbitrary window performance into an equivalent single layer.

2.3.5 Phase change material

The three BPS tools implement different approaches and models to predict the latent heat storage in a PCM layer. In particular, the models implemented are the lumped method coupled with the quasi-heat source method for Type 1270 of TRNSYS, the enthalpy method for EnergyPlus and the enthalpy method with hysteresis for IDA ICE.

Type 1270 [25] is a very simple PCM model: it is designed to interact with Type 56 (building model) when the PCM layer is integrated into an internal wall that is in contact on both boundary surfaces with a thermal zone. Consequently, Type 1270 cannot be used when the PCM layer is in direct contact with thermal air node and the wall is in contact with the outdoor environment.

The wall containing the PCM is split into two parts (see Figure 6) consisting of only standard layers: one located on the right side and the other one on the left side of the PCM layer. Type 1270 models the PCM layer with a sole node, considers constant density, specific heat capacity and thermal conductivity with the temperature and in the two phases and, during the phase change phenomenon, constant melting/solidification temperature associated with a latent heat of fusion. Consequently, hysteresis and subcooling phenomena and the storage/release of the latent heat in a temperature range are excluded.

The Type 1270 has the task to calculate at each time step the PCM temperature as a function of the energies coming from the right and left side of the PCM layer $Q_{r,i}$ and $Q_{l,i}$, which in turn depend on the same PCM temperature. Then, a feedback loop at each time step is created, as shown in Figure 6, where the $Q_{r,i}$ and $Q_{l,i}$ outputs of Type 56 are sent as input to Type 1270. This Type returns the PCM temperature that is employed by Type 56 to calculate $Q_{r,i}$ and $Q_{l,i}$ as long as the convergence is reached.

Figure 6 - Model and simulation scheme in TRNSYS for the integration of a PCM layer into an opaque internal wall.

To calculate the PCM temperature three circumstances can be highlighted: when the PCM layer *a)* is totally liquid, *b)* totally solid or *c)* in phase change. Both in case a) and b), the PCM temperature at the successive time instant ${T_{PCM}}^{n+1}$ is calculated with the following equation:

$$ {T_{PCM}}^{n+1} = {T_{PCM}}^{n} + \left(\frac{{Q_{r,i}}^{n} + {Q_{l,i}}^{n}}{m_{PCM}\, c_{p,PCM}} \right) \tag{25} $$

Where, ${T_{PCM}}^{n}$ is the PCM temperature at the current time instant, m_{PCM} PCM mass, and $c_{p,PCM}$ PCM specific heat capacity at solid or liquid state. In the case c), during the phase change, the PCM temperature is maintained constant at own melting temperature and the latent heat of fusion is compared with the overall energy coming from both sides of the layer. If the PCM layer cannot totally store this energy since the PCM latent storage capacity has been exceeded, then the phase change process is complete and the energy in excess is attributed to sensible storage in the layer with the PCM temperature calculated with Eq. (25). If the overall energy coming from both sides of the layer can be totally stored by the PCM layer, then the overall energy absorbed or released is recorded and a new value of the liquid fraction is computed by maintaining the PCM temperature constant.

This Type cannot be used to simulate the STB in which a PCM layer is placed on the internal surface of the floor since the PCM is in direct contact with the thermal air node and the floor is an external wall.

For the scopes of this research, the Type 1270 functioning was modified, see Figure 7. The external wall is split again into two standard layers: on the outermost side, the standard layer is in direct contact with the outdoor environment while on the innermost side with the indoor environment. The energy coming from the right side $Q_{r,e}$ is calculated with Type 56 in a similar manner of the previous case. Instead, the energy coming from the left side $Q_{l,e}$ is calculated by solving the equivalent electric circuit that described the heat transfer from the outdoor environment until the PCM node. In particular, the electric circuit models all the thermal exchanges between the outdoor environment and the external surface wall and the heat conduction into the

wall until the PCM node by neglecting the sensible heat capacity. This assumption is as accurate as the thermal capacity of the left side of the wall is low.
For the purpose, a more complex feedback loop was created in TRNSYS by writing the mathematical expression of $Q_{l,e}$ in an "assembly equation" that requires as input the outdoor climate data and the PCM temperature. In turn, this temperature is calculated by Type 1270 starting from $Q_{l,e}$ and $Q_{r,e}$, which as usual is calculated by Type 56.

Figure 7 - Model, simulation and electrical circuit scheme in TRNSYS for the integration of a PCM layer into an opaque external wall.

The energy $Q_{l,e}$ was determined by means of the external surface heat balance of Eq. (26), while the external surface temperature in Eq. (27) was obtained by equaling $Q_{l,e}$ to the conductive heat flux between the external surface node and the PCM node.

$$Q_{l,e} = A\left[q_{sol,e} + h_{cv,e}\left(T_{a,e} - T_{s,e}\right) + h_{r,sky}\left(T_{sky} - T_{s,e}\right) + h_{r,grd}\left(T_{grd} - T_{s,e}\right)\right] = Q_{cd,e} \quad (26)$$

$$T_{s,e} = \frac{q_{sol,e} + h_{cv,e}T_{a,e} + h_{r,sky}T_{sky} + h_{r,grd}T_{grd} + \frac{T_{PCM}}{\sum_{j=1}^{z} R_j}}{h_{cv,e} + h_{r,sky} + h_{r,grd} + \frac{1}{\sum_{j=1}^{z} R_j}} \quad (27)$$

Where, T_{PCM} is the PCM nodal temperature and R_j is the j-th thermal resistance of the *z* layers on the right side of the wall.
When the PCM is placed on the internal or external surface in direct contact with the indoor or outdoor environment, the feedback loop proposed can still be used by introducing a virtual layer characterized by a very low thermal resistance and heat capacity.
For the STB with the PCM layer placed on the internal surface of the floor, a virtual layer was introduced on the internal surface put before the PCM layer.
EnergyPlus contains a more sophisticated model to predict the latent heat storage in a PCM layer. Compared to the Type 1270 model, the heat capacity method of EnergyPlus removes the assumption that the phase change phenomenon occurs at the specific melting temperature, as a pure material, but rather in a temperature range in which a variable heat capacity with the temperature is considered [19, 26, 27]. This heat capacity is detected at each time step from the enthalpy curve of the PCM layer with Eq. (28). EnergyPlus requires an only enthalpy curve to be used both in the fusion and solidification process.

$$C_{P,PCM} = \frac{\left(H_i^{n+1} - H_i^n\right)}{\left(T_i^{n+1} - T_i^n\right)} \quad (28)$$

The heat capacity is updated at each time step in Eq. (28) in the PCM nodes. Finally, EnergyPlus allows variation of thermal conductivity with temperature. As a consequence, it permits to set different thermophysical properties in the solid and liquid phase.

Until recently, IDA-ICE did not permit to simulate a PCM layer. In 2015, EQUA Simulation AB introduced the "PCM-WALL" which implements a modified enthalpy method to take into account with the hysteresis phenomenon [28]. In particular, compared to EnergyPlus, IDA ICE requires both the solidification and fusion enthalpy curves and the enthalpy H_i^{t+1} is not only dependent on the current state but also on the previous state. The hysteresis is modelled with a further variable named *mode* to detect five different physical states: *mode -2* solid phase; *mode 2* liquid phase; *mode -1* solidification phase; *mode 0* inversion

during the solidification/fusion process; *mode 1* fusion process. The heat capacity is determined as a function of the following variables:

$$C_{p,PCM} = f(T_i^{n+1}, T_i^n, \text{mode}) \quad (29)$$

Finally, IDA ICE considers different values of density and thermal conductivity in the liquid and solid phase and during the phase change, a mean value is considered.

2.3.6 Lesson learned: alignment of the three tools

To detect the actual accuracy of the three BPS tools in the comparison with the experimental results, some aspects require alignment in order to attribute the deviations in results only to the different accuracy of mathematical models implemented. In the building simulation setting, the aspects considered are the building geometric representation, the outdoor climate conditions, heat transfer parameters, and thermophysical properties of the PCM layer.

2.3.6.1 Building geometric representation

For the building 3D construction, TRNSYS employs a plug-in with Google Sketchup, EnergyPlus utilizes the DesignBuilder interface, while IDA ICE contains an integrated graphical interface, as shown in Figure 8.

Figure 8 - 3D solar test box in the real conditions a), built-in Google Sketchup for TRNSYS b), in DesignBuilder for EnergyPlus c) and in the IDA ICE interface d).

In Google Sketchup, starting from the net volume, all the external surfaces of the thermal zone are defined, see Figure 8b for the STB, while the setting of the wall thicknesses is made into TRnbuild starting from the internal surfaces. Consequently, the thermal zone volume and the internal surface areas are correctly represented, while the areas of external surfaces are lower than the actual ones. An identical approach is employed by IDA ICE; an STB 3D representation is highlighted in Figure 8d, with evidence as regards the neglecting of the actual external surface. Finally, DesignBuilder allows the user to choose: a gross, net, or also mean internal volume of the thermal zone; if the surface areas related to the internal side or external side of a wall are to be used. For the STB, the approach used in Google Sketchup and IDA ICE was replicated in Design Builder as shown n Figure 8c.

2.3.6.2 Outdoor climate conditions

As mentioned in Section 2.2, the experimental weather data useful for the STB thermal dynamic simulation are the external air humidity and temperature, normal direct solar radiation, horizontal diffuse solar radiation, and wind speed intensity and direction. In addition, the global solar radiation incident on the windowed vertical surface exposed to the south was measured.

Since the list of input weather data required by the three tools is different, a preliminary analysis was developed in order to calculate all the missing weather data starting from those available.

By means of the Types 33, in TRNSYS environment, all the psychometric parameters of the external air were calculated. Instead, the direct solar radiation on the horizontal plane was calculated starting from normal direct solar radiation through the determination of the incidence angle.

To generate the fictive sky temperature, see Eq. (30), the recent Daguenet model [29] was employed and imported in all three tools, except for EnergyPlus that requires the corresponding infrared radiation coming from the sky.

$$T_{sky} = T_{a,e}[(0.53 + 0.065{p_v}^{0.5})(1 - 0.1C) + 0.1C]^{0.25} \quad (30)$$

Where, C is the cloudiness degree calculated as a function of the ratio of diffuse and global solar radiation on the horizontal plane [30], and p_v vapour pressure function of the external air humidity and temperature.
All these data were employed to build the experimental *epw* file required by EnergyPlus. Instead, the data required by IDA ICE are those acquired experimentally. Since the ground temperature is assumed to be the same as the external air temperature in IDA ICE, the same approach was used also in EnergyPlus and TRNSYS.
Finally, to determine the global solar radiation on the STB surfaces differently oriented and inclined, the Perez model [31] for the diffuse component was selected in all the three tools. Since the opaque external walls are insulated, the main drive for the thermal exchange in STB thermal zone is the solar radiation entering through the windowed wall exposed to South. Since not all the tools permit to import the experimental values of the solar radiation on the inclined surfaces, verification was made. The global solar radiation on the southern orientation generated by the three tools was compared with that detected experimentally, as shown in Figure 9.

Figure 9 – Comparison of the experimental global solar radiation on the horizontal plate and that calculated with TRNSYS, EnergyPlus and IDA ICE.

The figure highlights that in all the three characteristic periods considered, the global solar radiation calculated by the three tools is very much in agreement with that experimentally detected, demonstrating the alignment of the three tools and Perez model accuracy.

2.3.6.3 Heat transfer parameters

As shown in Sections 2.3.1.1 and 2.3.2.1, IDA ICE employs specific models not changeable by the user to evaluate the external and internal convective heat transfer coefficients. In TRNSYS and EnergyPlus a value of 20 W/m^{2}K was used for the external surface, while on the internal surface, the value of 3 W/m^{2}K was used in EnergyPlus, and the internal calculation mode was active in TRNSYS. For the ground radiative heat transfer coefficient with the external surface of the STB floor value of $h_{r,grd}$= 5 W/m^{2}K was set.
For the distribution of direct solar radiation entering through the window onto the internal wall of the thermal zone, the detailed mode in EnergyPlus was chosen to align it with TRNSYS.
Finally, both in TRNSYS and EnergyPlus, the spectral and hemispherical optical properties of the window system and the optical properties as a function of the incidence angle were imported from WINDOW program. Instead, in IDA ICE, hemispherical constant values of the optical properties were associated.

2.3.6.4 PCM thermophysical properties

The parameters required by the PCM mathematical models implemented in the three tools were set in order to put them in similar conditions. The overall latent heat of fusion associated with the enthalpy curve, by excluding the sensible contribution, was set in TRNSYS in the phase change temperature range. Three different cases were considered by associating the melting peak temperature of 20 °C, the solidification peak temperature of 22 °C and the intermediate value of 21 °C as constant phase change temperature. On the other hand, three different enthalpy curves were set in EnergyPlus: the first one related to the fusion process, the second one related to the solidification process and the third one related to the mean values at each temperature calculated in the solidification and fusion processes. In IDA ICE, the solidification and fusion enthalpy curves were singularly imported.
As regards, the other PCM thermophysical properties, a mean value in the solid and liquid phase was considered in TRNSYS, while they were set differently in the two phases in IDA ICE and EnergyPlus.

2.4 *Accuracy indices*

As mentioned in Section 2.2, the experimental inner and outer surface glass temperatures, indoor air temperature, and internal surface floor temperature, for both the reference and PCM-based STBs, are used to estimate the accuracy of the three tools considered. For this purpose, three accuracy indices were calculated for each short-time experimental campaign and for each experimental measurement. The indices employed are the coefficient of determination R^2, Eq. (31), root mean square error RMSE, Eq. (32), and normalized RMSE, Eq. (33).

$$R^2 = 1 - \frac{\sum_{i=1}^{N}(m_i - s_i)^2}{\sum_{i=1}^{N}(m_i - \bar{m})^2} \tag{31}$$

Where, m_i is the i-th data measured, s_i is the i-th data simulated by the tools, $\bar{m}$ is the mean of the measured data and N is the number of data. R^2 closer to one indicates that the tool correctly predicts the data sample values.

$$RMSE = \sqrt{\frac{\sum_{i=1}^{N}(m_i - s_i)^2}{N}} \tag{32}$$

RMSE varies between zero and one: a value closer to zero indicates an absence of deviations between measured and simulated data.

The normalized RMSE NRMSE, compared to the measured mean value $\bar{m}$, facilitates the comparison between measured and simulated values with different scales.

$$NRMSE = \frac{RMSE}{\bar{m}} \tag{33}$$

Finally, a comprehensive accuracy metric is defined to provide a rank between the three BPS tools. In an analogous manner of the procedure proposed by Zhou [32], a sole accuracy index calculated starting from the R^2 and RMSE was used. The NRMSE was not considered since has the same qualitative behaviour of the associated RMSE. First of all, for each couple of R2 and RMSE, namely for the c-th case (corresponding to a fixed BPS tool, measured temperature and measurement period), standardization is required to make them both variable between 0 and 1, as reported in Eq. (34).

$$\begin{cases} \boldsymbol{r2_c = \frac{R2_c - R2_c^{min}}{R2_c^{max} - R2_c^{min}}} \\ \boldsymbol{rmse_c = \frac{RMSE_i^{max} - RMSE_i}{RMSE_c^{max} - RMSE_c^{min}}} \end{cases} \tag{34}$$

Where, $r2_c$ and $rmse_c$ are the standardized values of R2 and RMSE, $\boldsymbol{R2_c^{max}}$ and $\boldsymbol{RMSE_c^{max}}$, and $\boldsymbol{R2_c^{min}}$ and $\boldsymbol{RMSE_c^{min}}$ are, respectively, the corresponding maximum and minimum values obtained in the different cases.

The expressions for $r2_c$ and $rmse_c$ are different since the RMSE accuracy decrease as their values increase, the distribution with the smallest values on these metrics will have a normalized value of one. Meanwhile, the R2 accuracy, increase as their values increase, thus the distribution model with the largest values on these statistics will have a normalized value of one.

The accuracy index AI_c for the c-th case, namely for a specific BPS tool, measured temperature and measurement period, is the weighted sum of the standardized r2 and rmse and it is defined in the following equation:

$$\boldsymbol{AI_c = r2_c w_{r2} + rmse_c w_{rmse}} \quad (35)$$

Where, $\boldsymbol{w_{r2}}$ and $\boldsymbol{w_{rmse}}$ are respectively the r2 and rmse weights, of which sum is one.
Finally, the overall accuracy index AI in the different measurement periods p, namely for a specific BPS tool and measured temperature, is calculated as a weighted sum of the accuracy indices AI_c with identical weight:

$$\boldsymbol{AI = \frac{1}{P}\sum_{c=1}^{P} AI_c} \quad (36)$$

3 Results

3.1 *Solar test box without PCM*

3.1.1 Accuracy of the three tools

Figures 10-12 show, for the experimental campaigns made respectively in September, November and December on the reference STB, the comparison between experimental and simulated trends of the internal air temperature, and glass internal and external surface temperatures respectively from the top to the bottom.

Figure 10 – Comparison of the experimental and simulated trends of the internal air temperature, and glass internal and external surface temperatures in September for the reference STB.

Figure 11 – Comparison of the experimental and simulated trends of the internal air temperature, and glass internal and external surface temperatures in November for the reference STB.

Figure 12 – Comparison of the experimental and simulated trends of the internal air temperature, and glass internal and external surface temperatures in December for the reference STB.

For reference STB, the results of the BPS tools are particularly overlapped with each other and with experimental trends, demonstrating an excellent agreement. In general, for the internal air temperature and glass internal surface temperature, the slight deviations between simulated and experimental trends are to be associated with the values attributed to some thermal quantities, such as the internal convective heat transfer coefficient and sky temperature. In particular, these quantities were modelled with appropriate models since experimental data to be provided to the tools were not available. In addition, the infiltration flow rates, assumed constant and equal to 0.5 vol/h, are variable in time as a function of the intensity and direction of the wind speed. For this reason, a further analysis was conducted to evaluate the impact of the air infiltration flow rates on the internal air temperature trend by considering a variation range between 0 vol/h and 3 vol/h. In particular, only the TRNSYS tool was used since the results of the three tools are comparable. Figure 13 highlights the simulated internal air temperature trend modifications in comparison to the experimental one by varying the air infiltration flow rates. In the images, I0 and I30 indicate, respectively, the simulated internal air temperature by setting 0 vol/h and 3 vol/h.

Figure 13 – Simulated internal air temperature trend for different air infiltration flow rates.

In all three periods, the air infiltration flow rate increase leads to a reduction of the internal air temperature during the daylight hours, while the effect produced on the nocturnal internal air temperature is negligible, being the internal air temperature very close to the external one since the envelope is almost devoid of thermal inertia. In the three periods, the value of air infiltration flow rate that permits to align the

experimental trend with the simulated one is different. This demonstrates that the air infiltration flow rate is variable during the time and the deviations observed are also to be attributed to the constant value set in the simulations.
In conclusion, the deviations observed during the daylight hours are to be attributed especially to the constancy and value set for the air infiltration flow rate, and, in a less extensive manner, also to the approaches used to model the optical and thermal transfer through glass system and to distribute the solar radiation into the STB. Instead, during the night hours, being the internal air temperature almost independent of infiltration flow rate, the deviations are mainly owing to the models used to calculate the variable internal convective heat transfer coefficient, sky temperature and to the conductive heat transfer model in the walls. These models are also responsible for the slight differences between the results of the three tools. Similar considerations way can be extended also to the glass internal surface temperature.
The measurements show generally also larger surface temperatures on the exterior side of the window exposed to the South than what was simulated. At the same time, there is an excellent agreement between the simulated and measured global radiation on the southern exposure for the same period. The TT500 thermistor located on the outer side of the glass has been fixed to the glass using a high reflective aluminium tape in order to reduce the solar radiation influence on the temperature measurement. However, this precaution did not completely prevent the sensor heating caused by the incident solar radiation and the measurement to be affected by a systematic error as evidenced by the comparison with the simulated temperature profiles.
To highlight this phenomenon, Figure 14 shows how the systematic error (ΔT, the difference between experimental and simulate internal air temperature) changes as a function of the global solar radiation incident of the southern wall Gs by considering, for each simulation tool, data of all the three periods considered.

Figure 14 - Systematic error for each tool on the glass exterior surface temperature as a function of the incident global solar radiation on the southern wall by considering data of all the three periods considered.

As it can be noticed, an increase of the incident solar radiation leads to a growth of the systematic error demonstrating how, in this case, the tools are more accurate than the experimental measures. However, these measurements are a useful reference to validate the simulations, especially during the nocturnal hours. In fact, as can be observed in the images, for all three tools, the absence of solar radiation during the nocturnal hours $G_s=0$ leads to the least deviation ΔT, which is very close to zero.
Figures 15-17 report, for the experimental campaigns made respectively in September, November and December on the reference STB, the values of R^2, RMSE and RMSE calculated by the three BPS tools for each measured temperature.

Figure 15 – Accuracy indices in September for the reference STB.

Figure 16 – Accuracy indices in November for the reference STB.

Figure 17 – Accuracy indices in December for the reference STB.

From a quantitative point of view, TRNSYS and EnergyPlus highlight generally the best accuracy to determine the glass internal and external surface temperatures owing to the more sophisticated models used than that used by IDA ICE. Generally, in the absence of the PCM module, the three BPS tools show high accuracy and can be considered comparable if the internal air temperature is used for the comparison.
Globally,

- for the internal air temperature in September, the lowest RMSE and NRMSE of 2.027 °C and 7.522% is obtained by using TRNSYS, in November and December, the minimum RMSE values of 2.038 °C and 2.374 °C, minimum NRMSE of 10.367 % and 18.905 %, and maximum R^2 of 0.975 and 0.984 occur always by employing IDA ICE.
- for the glass internal surface temperature, TRNSYS highlights the minimum RMSE of 2.364 °C in September and the minimum NRMSE of 9.493 %, IDA ICE leads to the lowest values of RMSE and RMSE in November and December, instead, EnergyPlus shows the highest R^2 in September and November.
- for the glass external surface temperature, IDA ICE guarantees always the minimum RMSE and NRMSE values and the maximum R^2 values.

3.2 *Solar test box with PCM*

3.2.1 Effect of the melting temperature in TRNSYS

When the test box is equipped by the PCM module, TRNSYS permits to set a latent heat of fusion/solidification at a specific phase change temperature, by neglecting the phase change temperature range. To identify the best phase change temperature in the prediction of the experimental data, a preliminary investigation was developed by varying the phase change temperature from 20 °C to 22°C. Table 4 reports for each experimental campaign period the accuracy index AI_i and the overall AI obtained for the different measured temperatures.

Table 4 – Accuracy index and overall accuracy index by varying the phase change temperature in TRNSYS.

The table highlights the different optimal phase change temperatures by considering the different measured temperatures. For the aim of this section, the best phase change temperature must be selected by considering the most representative measure for the phase change phenomenon detection. By employing the PCM floor internal surface temperature, the highest overall accuracy index was obtained with a phase change temperature of 21 °C, the intermediate value between the peak phase change temperature of the heating and cooling h-T curves. This value is considered for the comparison with the other BPS tools.

3.2.2 Effect of the enthalpy-temperature curve in EnergyPlus

When the test box is equipped by the PCM module, EnergyPlus permits to set a sole enthalpy-temperature curve, by neglecting the hysteresis phenomena. To identify the best curve in the prediction of the experimental data, a preliminary investigation was developed by using the fusion, solidification and average enthalpy-temperature curve. Table 5 reports for each experimental campaign period the accuracy index AI_i and the overall AI obtained for the different measured temperatures.

Table 5 – Accuracy index and overall accuracy index by using the fusion, solidification and average enthalpy-temperature curve in EnergyPlus.

The table highlights the different optimal h-T curves by considering the different measured temperatures. For the aim of this section, the best phase change temperature must be selected by considering the most representative measure for the phase change phenomenon detection. By employing the PCM floor internal surface temperature, the highest overall accuracy index was obtained with the average h-T curve between the heating and cooling h-T curves. This curve is considered for the comparison with the other BPS tools.

3.2.3 Accuracy of the three tools

Figures 18-20 show, for the experimental campaigns made respectively in September, November and December on the PCM-based STB, the comparison between experimental and simulated trends of the internal air temperature, and glass internal and external surface temperatures respectively from the top to the bottom.

Figure 18 – Comparison of the experimental and simulated trends of the internal air temperature, glass internal and external surface temperatures, and PCM floor internal surface temperature in September for the PCM STB.

Figure 19 – Comparison of the experimental and simulated trends of the internal air temperature, glass internal and external surface temperatures, and PCM floor internal surface temperature in November for the PCM STB.

Figure 20 – Comparison of the experimental and simulated trends of the internal air temperature, glass internal and external surface temperatures, and PCM floor internal surface temperature in December for the PCM STB.

The PCM placed on the floor allows the STB to dampen the temperature fluctuation both in summer and winter period. In particular, the thermal excursion of the internal air temperature, the difference between the maximum and minimum temperature, is reduced from 44°C to 35 °C, from 38°C to 26 °C, and from 49 °C to 36°C respectively in September, November and December.
The surface floor temperature establishes that:

- in September, the PCM panel is prevalently in the liquid phase and a solidification process occurs during the late evening of each day when the external air temperature decreases and solar radiation is nil. This process does not complete because the cooling effect produced by the external longwave radiation and convective is not enough, and the PCM panel recovers the liquid phase in the morning.
- In November, the PCM is always in phase change with partial fusions and solidifications.
- In December, the PCM panel is always solid in the cloudy day, while it stores the solar radiation passing through the window incident on the floor in the other days allowing a complete phase change from the solid phase to the liquid phase. This process starts in the late morning and ends in the late afternoon when the PCM return in the solid phase releasing all the latent heat stored.

Overall, in the cold periods, the weather conditions and the phase change temperature allows exploiting the phase change better than the warm season. Consequently, the major deviations between the three BPS tools can be mainly appreciated in December and November owing to the different hypothesis formulated in the model definition. In particular, the effect of the constant melting temperature of the TRNSYS model can be highlighted by observing the higher internal air temperature during the solidification process and the lower internal air temperature during the fusion process. This is a consequence of the floor surface temperature that is constrained to remain constant, by influencing the internal air temperature, even when, during the fusion process, the floor temperature should be increased and during the solidification process should be decreased. As demonstrated by the results in terms of PCM surface temperature, the assumption described in Section 2.3.5, related to the absence of thermal capacity in the outermost side of the floor needed for the adaptation of the Type 1270 in TRNSYS to predict the thermal behaviour of a PCM placed into an external wall, can be retained acceptable. In fact, the insulation and plywood layers have a very low thermal capacity. Consequently, the deviations observed compared with the results of the other tools are to be associated with only the hypothesis of the simplified model incorporated into Type 1270 for the PCM layer in TRNSYS.

At the end of the phase change process, all the three tools are again overlapped since the latent heat stored and released only depends on the thermal power quantity incident the floor.
Instead, the EnergyPlus model tends to provide lower air internal temperature than the experimental ones during the solidification process because a unique enthalpy-temperature function for the heating and cooling process was introduced. In this way, if the sole fusion curve or a mean curve is set, the material completes the solidification process before owing to the higher value of phase change temperatures. The deviation to the experimental trend depends on the difference between the solidification and fusion latent heat, namely on the hysteresis phenomenon.
Finally, the enthalpy hysteresis model of IDA ICE allows obtaining the best prediction of the thermal behaviour of the PCM STB from a qualitative point of view.
Figures 21-23 report, for the experimental campaigns made respectively in September, November and December on the PCM-based STB, the values of R^2, RMSE and RMSE calculated by the three BPS tools for each measured temperature.

Figure 21 – Accuracy indices in September for the PCM STB.

Figure 22 – Accuracy indices in November for the PCM STB.

Figure 23 – Accuracy indices in December for the PCM STB.

The experimental trend of the PCM floor internal surface temperature is missing in September, while the glass internal surface temperature is missing in November and December since the thermistor placed on the glass internal surface of the PCM-base STB in September successively was moved on the PCM floor internal surface. The symbol N.A. is used to report the missing data.
From a qualitative point of view, IDA ICE is generally the best tool to predict the PCM-based STB. The PCM floor internal surface temperature highlights the highest accuracy of IDA ICE compared to the other BPS tools since the accuracy indices are very different. This difference between IDA ICE and the other BPS tools is also present for the other measured temperatures, although it is less significant.
Globally, IDA ICE highlights the lowest RMSE and NRMSE values and the highest R^2 values in all periods for all measured temperatures, except for the internal air temperature in September for which EnergyPlus provides the minimum RMSE value of 2.443 °C. It is worth mentioning the significant reduction of the R^2 and increase of the RMSE and NRMSE values for EnergyPlus and, especially, TRNSYS by comparing data with those of the case in the absence of PCM.

3.3 Overall accuracy index and BPS tool ranking

To complete the analysis and to establish a ranking among the BPS tools, both for the reference and PCM-based STB, the accuracy index was calculated for each experimental campaign period, BPS tool and measured temperature, while the overall accuracy index for each BPS tool and measured temperature. The results for the reference and PCM-based STB are respectively reported in Tables 6 and 7.

Table 6 – For the reference STB, accuracy index and overall accuracy index for the three BPS tools.

Table 7 – For the PCM-based STB, accuracy index and overall accuracy index for the three BPS tools.

In the absence of PCM, Table 6 highlights that the three BPS tools are strongly comparable and the best one depends prevalently on the experimental campaign period. In fact, in the warm period, TRNSYS assumes the highest accuracy indices, while in the cold periods IDA ICE leads to the highest accuracy indices. Instead, if the overall accuracy index is considered, IDA ICE is the best tool in all periods.

In the presence of PCM, Table 7 shows that IDA ICE guarantees almost the same accuracy obtainable in the absence of PCM, while the other tools provide lower accuracies. Consequently, in this case, IDA ICE is strongly recommendable for dynamic simulation, followed with a lower accuracy by EnergyPlus. Finally, TRNYS leads to the worst accuracy owing to the least sophisticated PCM model used.

4 Conclusions

This paper proposes a comparison between the most popular building performance simulation tools, EnergyPlus, IDA ICE and TRNSYS, with the experimental data provided by two STBs, devoid of and equipped with a PCM module on the floor, in three different warm, intermediate, and cold periods. Measurements of the internal air temperature, glass internal and external surface temperature and floor internal surface temperature are used for this purpose.

A comprehensive examination of the mathematical models used by the BPS tools considered was carried out related to the conductive, convective and longwave and shortwave heat exchanges between the envelope and the indoor and outdoor environment. TRNSYS and EnergyPlus can be considered the most sophisticated in the modelling of direct solar radiation passing through the window since it considers variable optical properties with incidence angle and TRNSYS also in terms of treatment of direct and diffuse solar radiation distribution into a zone. Contrarily, IDA ICE does not take into account the directionality effects of direct solar radiation, while EnergyPlus is the least accurate from a point of view of diffuse solar radiation modelling into a thermal zone. However, IDA ICE and EnergyPlus contain PCM models much more accurate than that of TRNSYS, which was modified to predict the thermal behaviour of a PCM also incorporated in an external wall.

For reference STB, the results of the BPS tools are particularly overlapped with each other and with experimental trends, demonstrating an excellent agreement. The slight deviations observed between experimental and simulated trends are to be associated with the setting of some thermal quantities not easily detectable experimentally, such as the infiltration flow rate, internal and external convective surface heat transfer coefficient, sky temperature, and with the measurement error of sensors.

Instead, in the presence of PCM, the three tools provide different agreement according to the tool employed.

Overall, the considerations and comparisons made on the employed mathematical models by the three tools find confirmation in the experimental investigation made:

- for the reference STB, TRNSYS leads to the best prediction in September, when the directionality effects of the solar radiation through the windowed wall are very incisive in the calculation of the thermal response of the zone owing to the high incident angle caused by the high sun elevation angle that produces a strong variation of the glass optical properties;
- for the PCM STB, IDA ICE turned out the most accurate tool since, owing to the small dimensions of the STB, the latent storage phenomenon is predominant compared the other heat transfer mechanisms in the determination of the internal air temperature.

The research has provided, by means of the use of standard statistical metrics, a ranking between the BPS tools, by evaluating RMSE, NRMSE and R^2 for the STB devoid of PCM and that including the PCM panel.

The use of the accuracy index by varying the experimental period and the overall accuracy overall proposed led to the following conclusions:

- In the absence of PCM, the three BPS tools are strongly comparable and the best one depends prevalently on the experimental campaign period. In fact, in the warm period, TRNSYS assumes the highest accuracy indices, while in the cold periods IDA ICE leads to the highest accuracy indices. Instead, if the overall accuracy index is considered, IDA ICE is the best tool in all periods.
- In the presence of PCM, IDA ICE guarantees almost the same accuracy obtainable in the absence of PCM, while the other tools provide lower accuracies. Consequently, in this case, IDA ICE is strongly recommendable for dynamic simulation, followed with a lower accuracy by EnergyPlus. Finally, TRNYS leads to the worst accuracy owing to the least sophisticated PCM model used. However,

although it does not allow temperature trends during the phase change to be predicted exactly, it allows the overall latent heat stored and released to be computed enough accurately by requiring only a few thermophysical data and the lowest computational cost.

Nomenclature

Symbols

a, b, c	constants for convective heat (-)
a_s, b_s, c_s and d_s	conduction coefficients
A	diagonal matrix of internal surface area (m^2)
A_g	glass surface (m^2)
A_i	i-th internal surface area (m^2)
AI	overall accuracy index (-)
AI_c	accuracy index of the c-th case (-)
$c_{p,PCM}$	PCM specific heat capacity at solid or liquid state (J/kgK)
C	cloudiness degree (-)
C_a	air heat capacity (J/K)
C_p	material heat capacity at constant pressure (J/K)
F	view factor matrix (-)
F_{air}	air view factor (-)
F_{grd}	ground view factor (-)
$F_{i,j}$	ScriptF coefficient between surfaces i e j
F_{sky}	sky view factor (-)
G_b	beam, solar radiation on the inclined surface (W/m^2)
G_d	diffuse solar radiation on the inclined surface (W/m^2)
G_{difsol}	solar Gebhart matrix (-)
G_r	reflected solar radiation on the inclined surface (W/m^2)
G_{lw}	Gebhart matrix (-)
$h_{cv,e}$	external surface convective heat transfer coefficient (W/m^2K)
$h_{cv,i}$	internal surface convective heat transfer coefficient (W/m^2K)
$h_{r,grd}$	ground radiative heat transfer coefficient (W/m^2K)
$h_{r,sky}$	sky radiative heat transfer coefficient (W/m^2K)
H	enthalpy (J/kg)
I_{difsol}	diffuse solar radiation transmitted through the window surface (W/m^2)
k	material thermal conductivity (W/mK)
K	constant for convective heat ($W/m^2K^{1/m}$)
$\bar{m}$	mean of the measured data
m_i	i-th data measured
m_{PCM}	PCM mass (kg)
N	number of data
NRMSE	normalized RMSE (-)
p	number of previous time instants (-)
p_v	vapour pressure (Pa)
$psi_{lw,i}$	net longwave absorption matrix (-)
psi_{sw}	net shortwave net absorption matrix (-)
P	number of experimental campaign periods (-)
q	heat flux (W/m^2)

q'_f	surface heat flux from the floor devoid of PCM (W/m^2)
$q_{cv,e}$	convective heat flux to the external air (W/m^2)
$q_{cd,e}$	conduction heat flux through the wall at the interface with the outdoor environment (W/m^2)
$q_{cv,i}$	convective heat flux to zone air (W/m^2)
$q_{cd,i}$	conduction heat flux through the wall at the interface with the zone air (W/m^2)
$q_{lw,air}$	longwave radiative exchange with the air (W/m^2)
$q_{lw,grd}$	longwave radiative exchange with the ground (W/m^2)
$q_{lw,e}$	net longwave radiation heat flux exchange with the surroundings (W/m^2)
$q_{lw,i}$	net longwave radiant exchange heat flux between zone surfaces (W/m^2)
$q_{lw,sky}$	longwave radiative exchange with the sky (W/m^2)
q_{PCM}	PCM floor surface heat flux (W/m^2)
$q_{sol,e}$	direct and diffuse solar radiation absorbed by the external surface (W/m^2)
$q_{sol,i}$	transmitted solar radiation through the windows absorbed by the internal surface (W/m^2)
Q_{difsol}	diffuse solar radiation in the cavity (W)
Q_e	convective gain from the eastern internal surface (W)
Q_f	convective gain from the floor internal surface (W)
$Q_{g,i}$	convective gain from the glass internal surface (W)
Q_{inf}	infiltration heat gain (W)
$Q_{l,i}$	energy coming from the left side of the PCM layer (J)
$Q_{lw,i}$	net absorbed longwave radiant heat flux between zone surfaces (W)
$Q_{lw,ij}$	net longwave radiation exchange between the surface i and surface j
Q_n	convective gain from the northern internal surface (W)
Q_r	convective gain from the roof internal surface (W)
$Q_{r,i}$	energy coming from the right side of the PCM layer (J)
$Q_{s,i}$	convective gain from internal surfaces (W)
Q_s	convective gain from the southern internal surface (W)
Q_{STB}	overall STB convective thermal power (W)
Q_w	convective gain from the western internal surface (W)
r	density (kg/m^3)
r2	standardized R^2 (-)
rmse	standardized RMSE (-)
R^2	coefficient of determination (-)
R_j	j-th thermal resistance (m^2K/W)
RMSE	root mean square error (-)
s_i	i-th data simulated
S_f	floor surface (m^2)
S_{PCM}	PCM floor surface (m^2)
t	time (s)
T	temperature (K)
$\widehat{T}$	internal surface temperature vector (K)
$T_{a,e}$	external air temperature (K)
$T_{a,i}$	internal air temperature (K)
T_{fsky}	fictive temperature of the surroundings (K)
T_{grd}	ground temperature (K)
T_i	i-th internal surface temperature (K)
T_j	j-th internal surface temperature (K)

T_{PCM}	PCM temperature (K)
$T_{s,e}$	external surface temperature (K)
$T_{s,i}$	internal surface temperature (K)
T_{sky}	sky temperature (K)
V	wind speed (m/s)
V_f	free stream wind speed (m/s)
w_{r2}	r2 weight (-)
w_{rmse}	rmse weight (-)
W_b	black body emissive power (W)
Y	constant for convective heat (-)
z	z-th layers (-)

Greek Symbols

α_e	absorptivity of the external surface (-)
α_i	absorptivity of the i-th internal surface (-)
Δt	time step (s)
Δx	space step in the wall (m)
ε_{lw}	longwave surface emissivity (-)
$\varepsilon_{s,e}$	emissivity of the external surface (-)
ε_{sw}	shortwave surface emissivity (-)
ρ_{lw}	longwave surface reflectivity (-)
ρ_{sw}	shortwave surface reflectivity (-)
σ	Stefan-Boltzmann constant (W/m^2K^4)

Superscripts

k	k-th previous time instants
min	minimum value
max	maximum value
n	n-th time instant

Subscripts

c	c-th case
i	i-th node of the wall
j	j-th node of the wall

Acknowledgement

This research has been carried out within the "Renovation of existing buildings in NZEB vision (nearly Zero Energy Buildings)" Project of National Interest (Progetto di Ricerca di Interesse Nazionale - PRIN) funded by the Italian Ministry of Education, Universities and Research (MIUR).

Author Contributions

Domenico Mazzeo played the main role since he conceived and designed the research, elaborated, interpreted and discussed the results data and contributed to the study of literature, to the study of the mathematical models of the three tools, to the simulations with TRNSYS and EnergyPlus tools, and to the preparation, writing and revising of the manuscript until the final publication. Nicoletta Matera contributed to the study of literature, and to the simulations with TRNSYS and EnergyPlus tools. Cristina Cornaro provided the experimental data, performed the simulations with IDA ICE tool and contributed to the study of the mathematical models of IDA ICE tool. Giuseppe Oliveti contributed to study the mathematical models of the three tools, and to the preparation, writing and revising of the manuscript until the final publication.

Piercarlo Romagnoni and Giuseppe Oliveti, coordinators of the UNICAL-IUAV group (Operative Unit 3 of the Project of National Interest), and Livio De Santoli, responsible for the Project of National Interest, coordinated the research team, administered project, acquired funding, provided supervision during the whole process, and read as well as approved the manuscript.

Conflicts of Interest: The authors declare no conflict of interest.

References

[1] International Energy Agency (2013). Transition to Sustainable Buildings, Strategies and Opportunities to 2050, Paris (France).

[2] International Energy Agency (2017). Global status report 2017, Towards a zero-emission, efficient, and resilient buildings and construction sector, Paris (France).

[3] Harish V.S.K.V., Kumar A. (2016). A review on modeling and simulation of building energy systems. Renewable and Sustainable Energy Reviews 56, 1272-1292.

[4] Saffari M., de Gracia A., Ushak S., Cabeza L. F (2017). Passive cooling of buildings with phase change materials using whole-building energy simulation tools: A review. Renewable and Sustainable Energy Reviews 80, 1239-1255.

[5] University of Wisconsin (2012). TRNSYS 17: A transien system simulation program. Solar Energy Laboratory. Available online: http://www.trnsys.com/ (accessed on 19 July 2019).

[6] Building Technologies Office of U.S. Department of Energy's (DOE) Building Technologies Office (BTO) (2016). EnergyPlus™ 8.6. Available online: https://energyplus.net/ (accessed on 19 July 2019).

[7] Equa Simulation AB (2018). IDA Indoor Climate and Energy 4.8. Available online: https://www.equa.se/en/ (accessed on 07 February 2019).

[8] TRANSSOLAR energietechnic GmbH (2012), TRNBuild 2.0, https://transsolar.com/ (accessed on 19 July 2019).

[9] DesignBuilder Software Ltd version 5.5.0 (2019). https://designbuilder.co.uk (accessed on 19 July 2019).

[10] Solar Energy Laboratory, University of Wisconsin-Madison (2012). TRNSYS 17 Documentation, Volume 5, Multi zone Building modeling with Type56 and TRNBuild.

[11] U.S. Department of Energy (2012). EnergyPlus™ Version 8.6 Documentation, Engineering Reference.

[12] Bring, A., Sahlin P., Vuolle M. (1999). Models for Building Indoor Climate and Energy Simulation, A Report of IEA SHC Task 22: Building Energy Analysis Tools, Subtask B: Model Documentation.

[13] Mazzeo, D., Oliveti, G., Arcuri, N. (2017). A method for thermal dimensioning and for energy behavior evaluation of a building envelope PCM layer by using the characteristic days. Energies, 10(5), 659.

[14] Mazzeo, D., Oliveti, G. (2018). Thermal field and heat storage in a cyclic phase change process caused by several moving melting and solidification interfaces in the layer. International Journal of Thermal Sciences 129, 462-488.

[15] Cornaro, C., Bucci, F., Pierro, M., Bonadonna, M. E., and Siniscalco, G. (2015). A new method for the thermal characterization of transparent and semi-transparent materials using outdoor measurements and dynamic simulation. Energy and Buildings 104, 57-64.

[16] Cornaro, C., Pierro, M., Puggioni, V. A., and Roncarati, D. (2017). Outdoor Characterization of Phase Change Materials and Assessment of Their Energy Saving Potential to Reach NZEB. Buildings 7(3), 55.

[17] Jayalath, A., Aye, L., Mendis, P., Ngo, T. (2016). Effects of phase change material roof layers on thermal performance of a residential building in Melbourne and Sydney. Energy and Buildings 121, 152-158.

[18] Panayiotou, G.P., Kalogirou, S. A., Tassou, S. A. (2016). Evaluation of the application of Phase Change Materials (PCM) on the envelope of a typical dwelling in the Mediterranean region. Renewable Energy 97, 24-32.

[19] Tabares-Velasco, P.C., Christensen, C., Bianchi, M. (2012). Verification and validation of EnergyPlus phase change material model for opaque wall assemblies. Building and Environment 54, 186-196.
[20] Rubitherm Technologies GmbH, Imhoffweg 6, 12307 Berlin (Germany). Available online: https://www.rubitherm.eu/ (accessed on 19 July 2019).
[21] Henninger, J. H. (1984). Solar Absorptance and Thermal Emittance of Some Common Spacecraft Thermal-Control Coatings (No. NASA-RP240400-1121). NATIONAL AERONAUTICS AND SPACE ADMINISTRATION WASHINGTON DC.
[22] Mazzeo, D., Oliveti, G., Arcuri, N. (2016). Influence of internal and external boundary conditions on the decrement factor and time lag heat flux of building walls in steady periodic regime. Applied Energy, 164, 509-531.
[23] Walton, G. N. (1983). Thermal Analysis Research Program Reference Manual. NBSSIR 83-2655. National Bureau of Standards.
[24] Lawrence Berkeley National Laboratory, USA (2017), WINDOW 7.6. https://windows.lbl.gov/software/window (accessed on 19 July 2019).
[25] TESS – Thermal Energy Systems Specialists (2010), TESSLibs 17, Component Libraries for the TRNSYS Simulation Environment, Volume A3 TESS Component Libraries.
[26] Pedersen, C.O. (2007). Advanced zone simulation in EnergyPlus: Incorporation of variable properties and Phase Change Material (PCM) capability. Proceedings of Building Simulation 2007.
[27] Wijesuriya, S., Brandt, M., Tabares-Velasco, P. C. (2018). Parametric analysis of a residential building with phase change material (PCM)-enhanced drywall, precooling, and variable electric rates in a hot and dry climate. Applied Energy 222, 497-514.
[28] Eriksson, L. (2015). CONTINUOUS_MODEL PCMWallH, PCM wall model with different temperature-enthalpy relations during melting and solidification. Hysteresis technique used to describe reversing during melting/solidification phase.
[29] Daguenet, M., (1985). Les séchoirs solaires: théorie et pratique. United Nations Educational, Scientific and Cultural Organization. Paris (France).
[30] Skartveit, A., Olseth, J.A., Czeplack, G., Rommel, M. (1996). On the estimation of atmospheric radiation from surface meteorological data. Solar Energy 56 (4) 349–359.
[31] Perez, R., Stewart, R., Seals, R., and Guertin, T., "The Development and Verification of the Perez Diffuse Radiation Model", Sandia Report SAND88-7030, (1988).
[32] Zhou, J., Erdem, E., Li, G., Shi, J. (2010). Comprehensive evaluation of wind speed distribution models: A case study for North Dakota sites. Energy Conversion and Management 51(7), 1449-1458.

Materials	**r** **kg/m^3**	**k** **W/mK**	**c_p** **J/kgK**	**ε** **-**	**α** **-**
Plywood	545	0.120	1215	0.900	0.200
Insulation	36	0.024	1453	0.900	0.500
Glass	2400	1.000	800	0.837	0.177
Air	1.2	0.0241	1005	-	-

Table 1: Thermophysical and optical properties of the wall layers of the solar test box.

SP21E thermophysical properties	Value
Specific heat capacity (kJ/kgK)	2.0
Solid density (at 15°C) (kg/l)	1.5
Liquid density (at 35°C) (kg/l)	1.4
Thermal conductivity (W/mK)	0.6
Maximum operation temperature (°C)	45

Table 2: Thermophysical properties of the PCM layer.

STB measurements	Device	Accuracy
Internal air temperature	TT500 thermistors	±0.2°C
External and internal surface temperature of the glass	TT500 thermistors	±0.2°C
Internal surface temperature of the floor	TT500 thermistors	±0.2°C
Weather measurements	**Device**	**Accuracy**
Normal direct solar radiation	Kipp&Zonen first class CH1 pyrheliometer mounted on a 2AP sun tracker	±2%
Horizontal diffuse solar radiation	Secondary standard CM21 shielded pyranometer mounted on a 2AP sun tracker	±3% a 1000 W/m^2
Global solar radiation on the vertical southern surface	silicon cell pyranometer	±5 %
External air temperature	Rotronic Hygroclip2 sensor	±0.1°C
External air humidity		±0.8 %
Wind speed intensity	model 7911 anemometer	±1 m/s
Wind speed direction		±7°

Table 3 – Measurement devices in the solar test box and outdoor environment.

	Phase change temperature 20 °C	Phase change temperature 21 °C	Phase change temperature 22 °C
Internal air temperature			
	Accuracy index AI_c		
September	0.673	0.674	0.670
November	0.773	0.811	0.823
December	0.619	0.625	0.630
	Overall accuracy index AI		
All	0.688	0.703	**0.708**
Glass internal surface temperature			
	Accuracy index AI_c		
September	0.805	0.804	0.801
November	N.A.	N.A.	N.A.
December	N.A.	N.A.	N.A.
	Overall accuracy index AI		
All	**0.805**	0.804	0.801
Glass external surface temperature			
	Accuracy index AI_c		
September	0.491	0.489	0.487
November	0.826	0.824	0.824
December	0.727	0.727	0.727
	Overall accuracy index AI		
All	**0.682**	0.680	0.679
PCM floor internal surface temperature			
	Accuracy index AI_c		
September	N.A.	N.A.	N.A.
November	0.449	0.417	0.310
December	0.209	0.256	0.303
	Overall accuracy index AI		
All	0.329	**0.337**	0.307

Table 4 – Accuracy index and overall accuracy index by varying the phase change temperature in TRNSYS.

	Fusion h-T curve	Solidification h-T curve	average h-T curve
Internal air temperature			
	Accuracy index AI_c		
September	0.795	0.835	0.811
November	0.925	0.935	0.934
December	0.812	0.821	0.817
	Overall accuracy index AI		
All	0.844	**0.864**	0.854
Glass internal surface temperature			
	Accuracy index AI_c		
September	0.833	0.861	0.847
November	N.A.	N.A.	N.A.
December	N.A.	N.A.	N.A.
	Overall accuracy index AI		
All	0.833	**0.861**	0.847
Glass external surface temperature			
	Accuracy index AI_c		
September	0.455	0.463	0.456
November	0.804	0.806	0.804
December	0.708	0.707	0.707
	Overall accuracy index AI		
All	0.656	**0.659**	0.656
PCM floor internal surface temperature			
	Accuracy index AI_c		
September	N.A.	N.A.	N.A.
November	0.766	0.675	0.755
December	0.568	0.593	0.589
	Overall accuracy index AI		
All	0.667	0.634	**0.672**

Table 5 – Accuracy index and overall accuracy index by using the fusion, solidification and average enthalpy-temperature curve in EnergyPlus.

	Internal air temperature			**Glass internal surface temperature**			**Glass external surface temperature**		
	IDA ICE	TRNSYS	EnergyPlus	IDA ICE	TRNSYS	EnergyPlus	IDA ICE	TRNSYS	EnergyPlus
AI_c									
September	0.875	**0.885**	0.786	0.792	**0.840**	0.824	**0.727**	0.633	0.601
November	**0.867**	0.729	0.695	**0.776**	0.725	0.693	**0.868**	0.800	0.774
December	**0.840**	0.684	0.611	**0.701**	0.672	0.605	**0.833**	0.704	0.675
AI									
All	**0.861**	0.766	0.697	**0.756**	0.746	0.708	**0.809**	0.712	0.684

Table 6 – For the reference STB, accuracy index and overall accuracy index for the three BPS tools.

	Internal air temperature			Glass internal surface temperature			Glass external surface temperature			PCM floor internal surface temperature		
	IDA ICE	TRNSYS	EnergyPlus	IDA ICE	TRNSYS	EnergyPlus	IDA ICE	TRNSYS	EnergyPlus	IDA ICE	TRNSYS	EnergyPlus
AI_c												
September	0.795	0.674	**0.811**	0.788	0.804	**0.847**	**0.604**	0.489	0.456	N.A.	N.A.	N.A.
November	**0.975**	0.811	0.934	N.A.	N.A.	N.A.	**0.868**	0.824	0.804	**0.894**	0.417	0.755
December	**0.846**	0.625	0.817	N.A.	N.A.	N.A.	**0.831**	0.727	0.707	**0.665**	0.256	0.589
AI												
All	**0.872**	0.703	0.854	0.788	0.804	**0.847**	**0.768**	0.680	0.656	**0.779**	0.337	0.672

Table 7 – For the PCM-based STB, accuracy index and overall accuracy index for the three BPS tools.

Figure 1 – Schematic view of the experimental and simulation campaign.

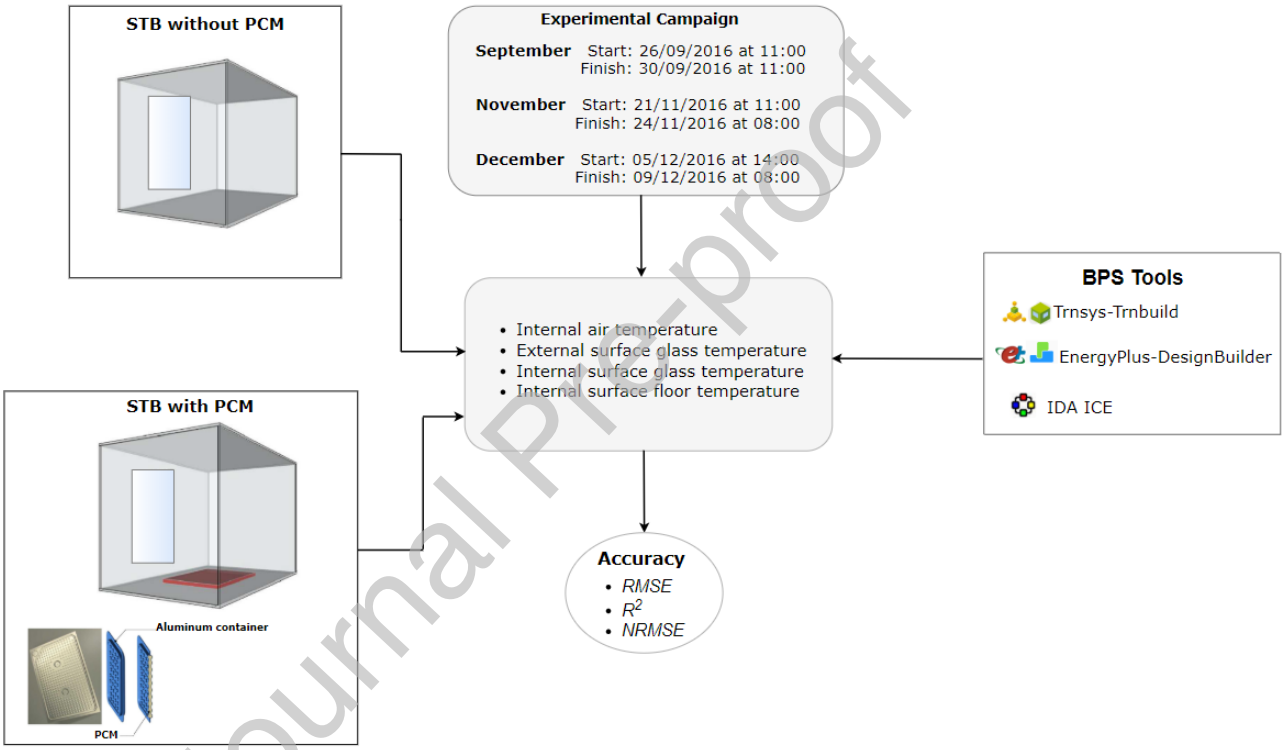

Figure 2 – Real 3D view, and 2D section planes and views of the PCM-based solar test box.

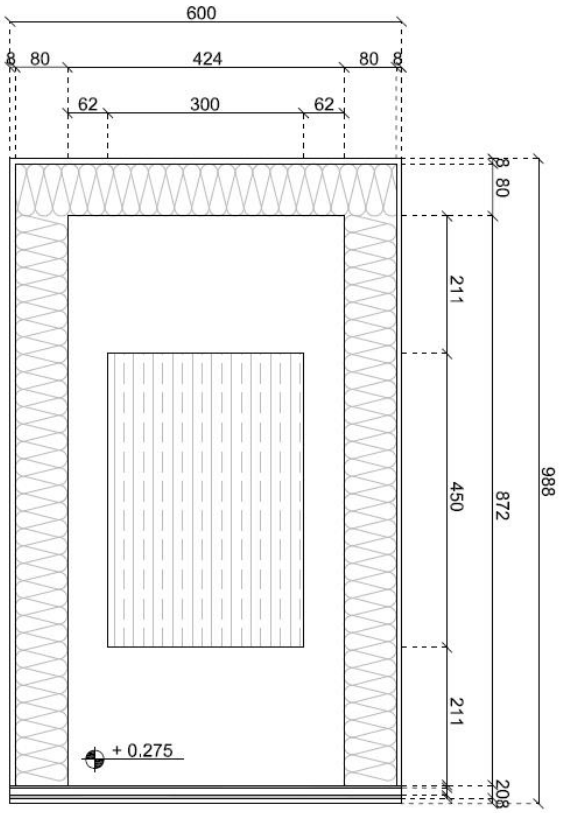

HORIZONTAL SECTION PLANE
SCALE 1:10

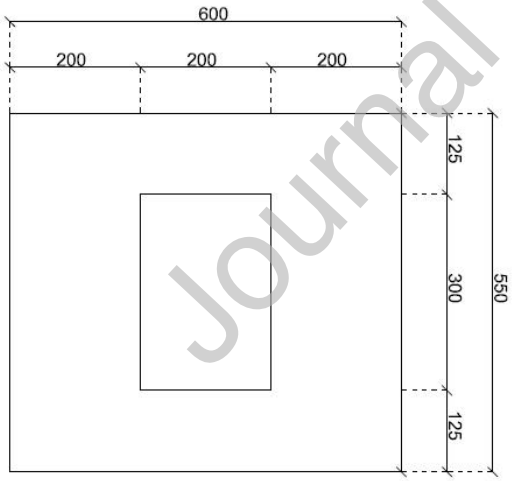

SOUTH PROSPECTUS
SCALE 1:10

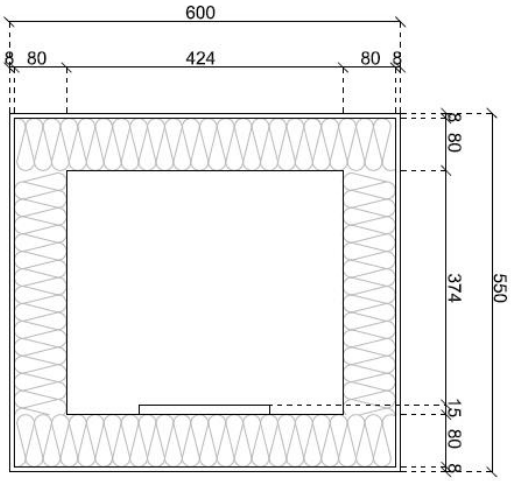

VERTICAL SECTION PLANE
SCALE 1:10

Figure 3 – Enthalpy and specific heat capacity as a function of the temperature for a heating and cooling process.

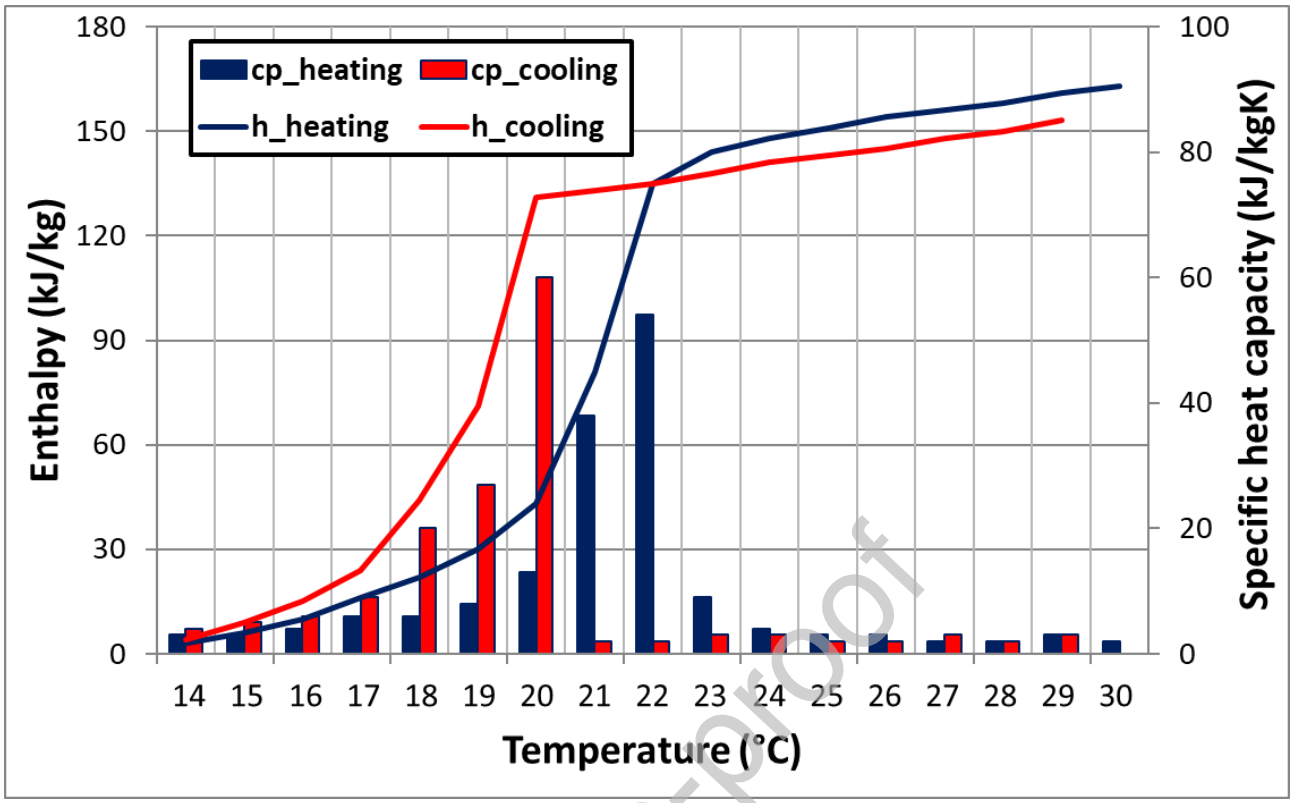

Figure 4 – Weather conditions in the three periods of the experimental campaign.

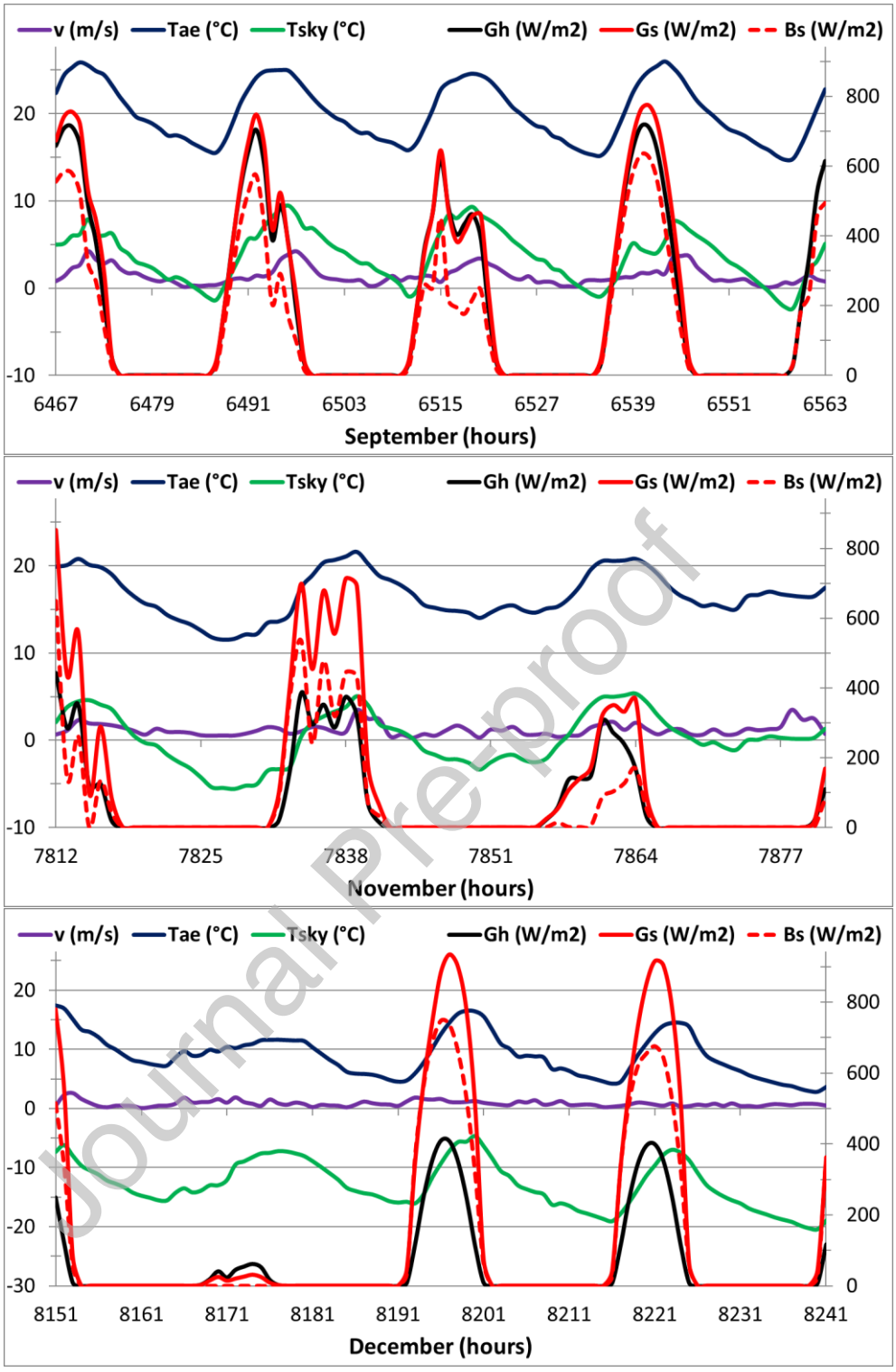

Figure 5 – Equivalent external air temperature in the three experimental campaigns compared with the melting and solidification peak temperatures.

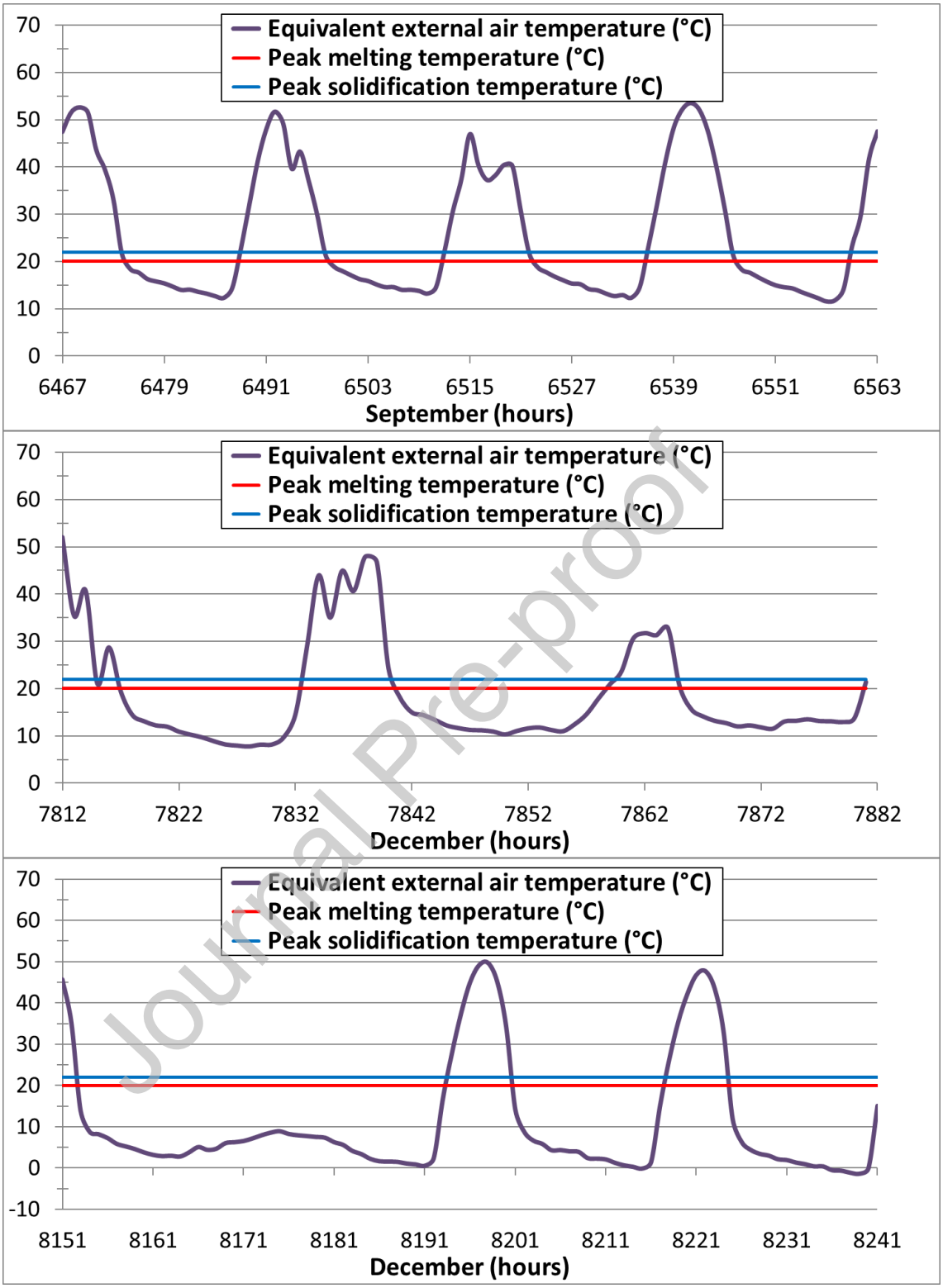

Figure 6 - Model and simulation scheme in TRNSYS for the integration of a PCM layer into an opaque internal wall.

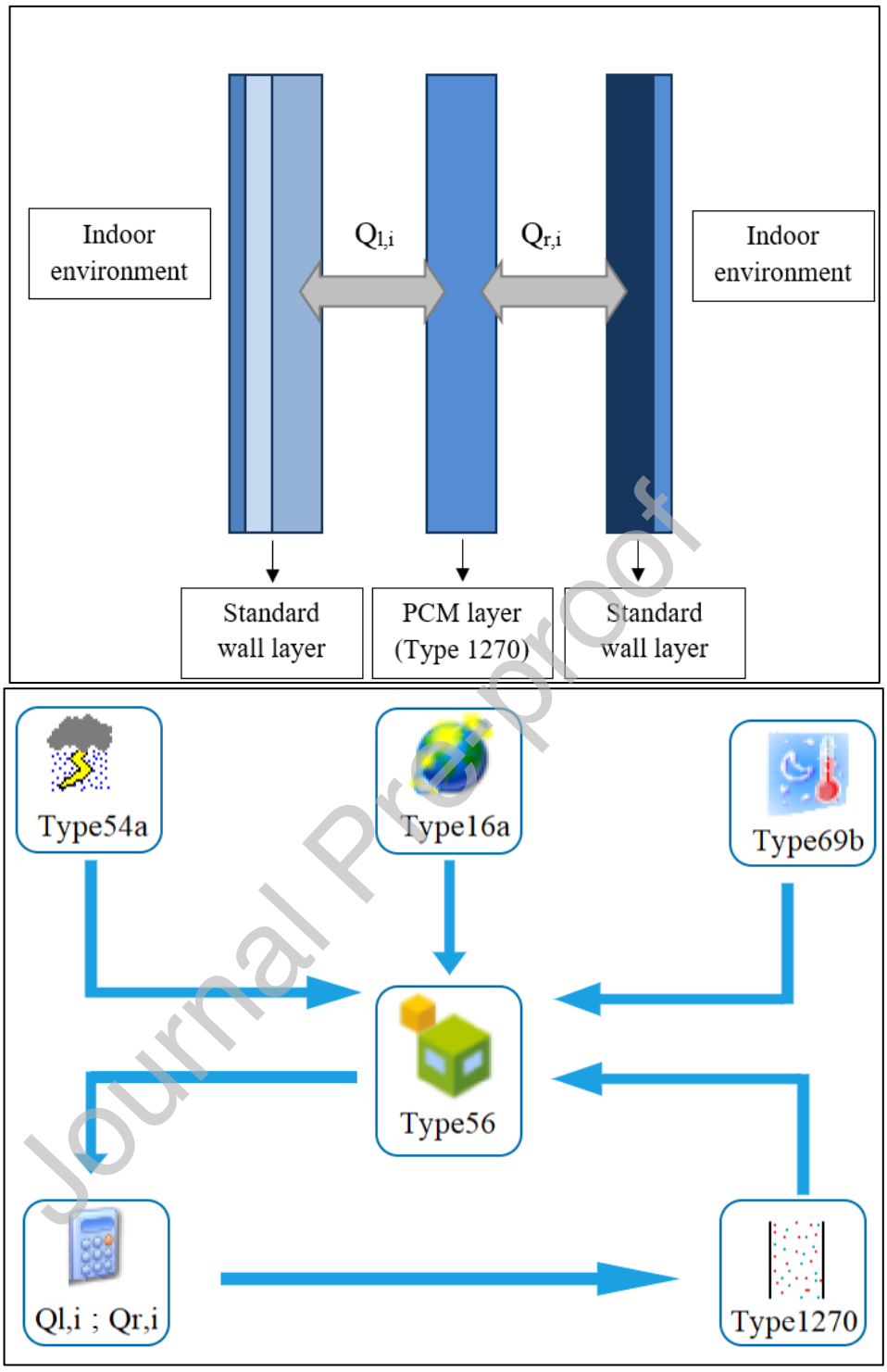

Figure 7 - Model, simulation and electrical circuit scheme in TRNSYS for the integration of a PCM layer into an opaque external wall.

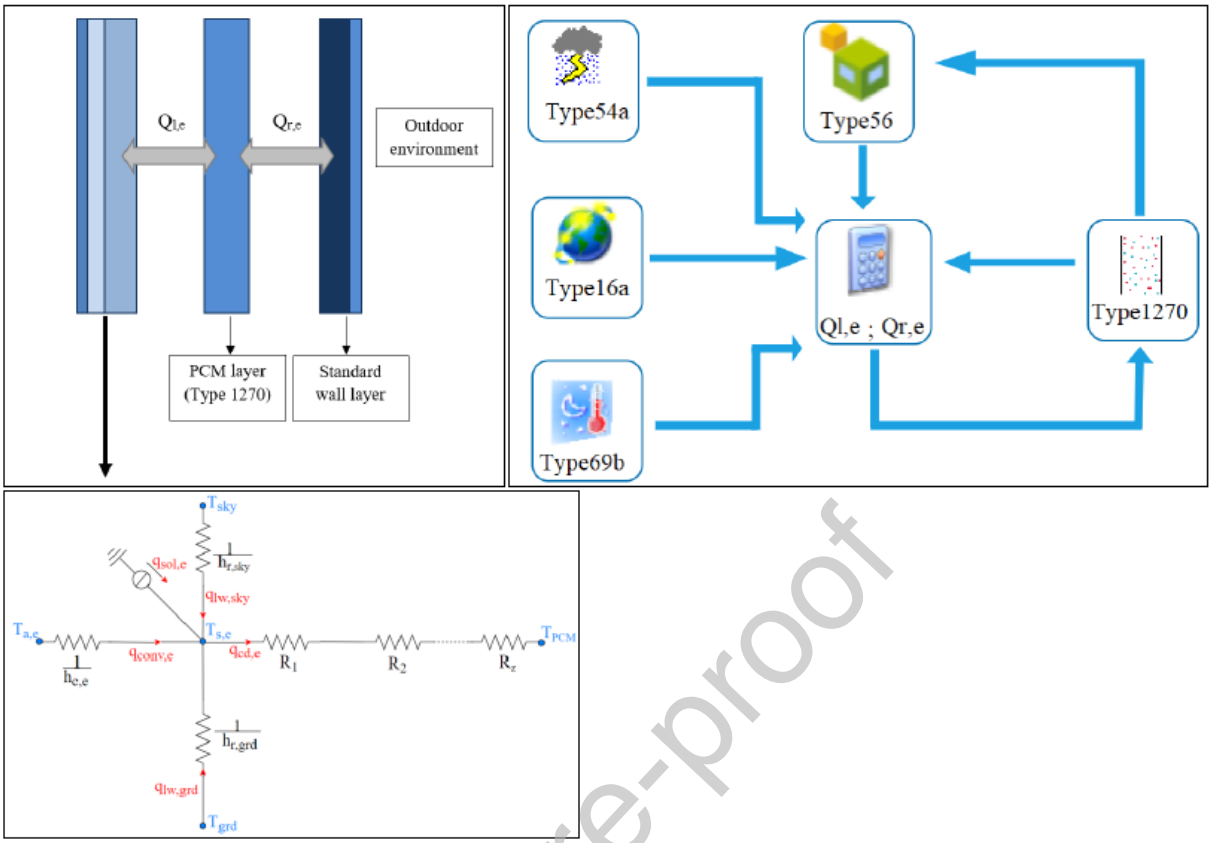

Figure 8 - 3D solar test box in the real conditions a), built-in Google Sketchup for TRNSYS b), in DesignBuilder for EnergyPlus c) and in the IDA ICE interface d).

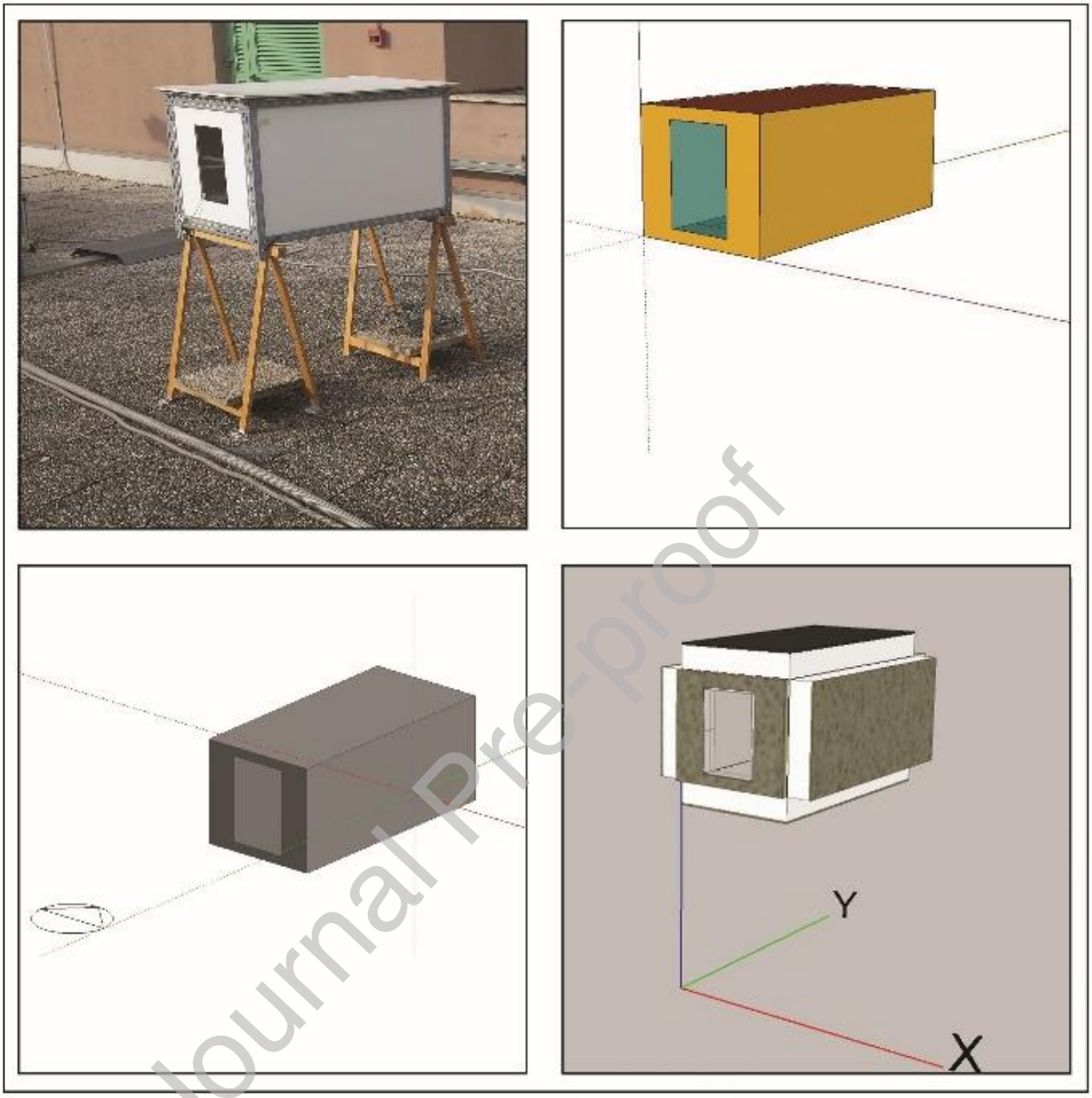

Figure 9 – Comparison of the experimental global solar radiation on the horizontal plate and that calculated with TRNSYS, EnergyPlus and IDA ICE.

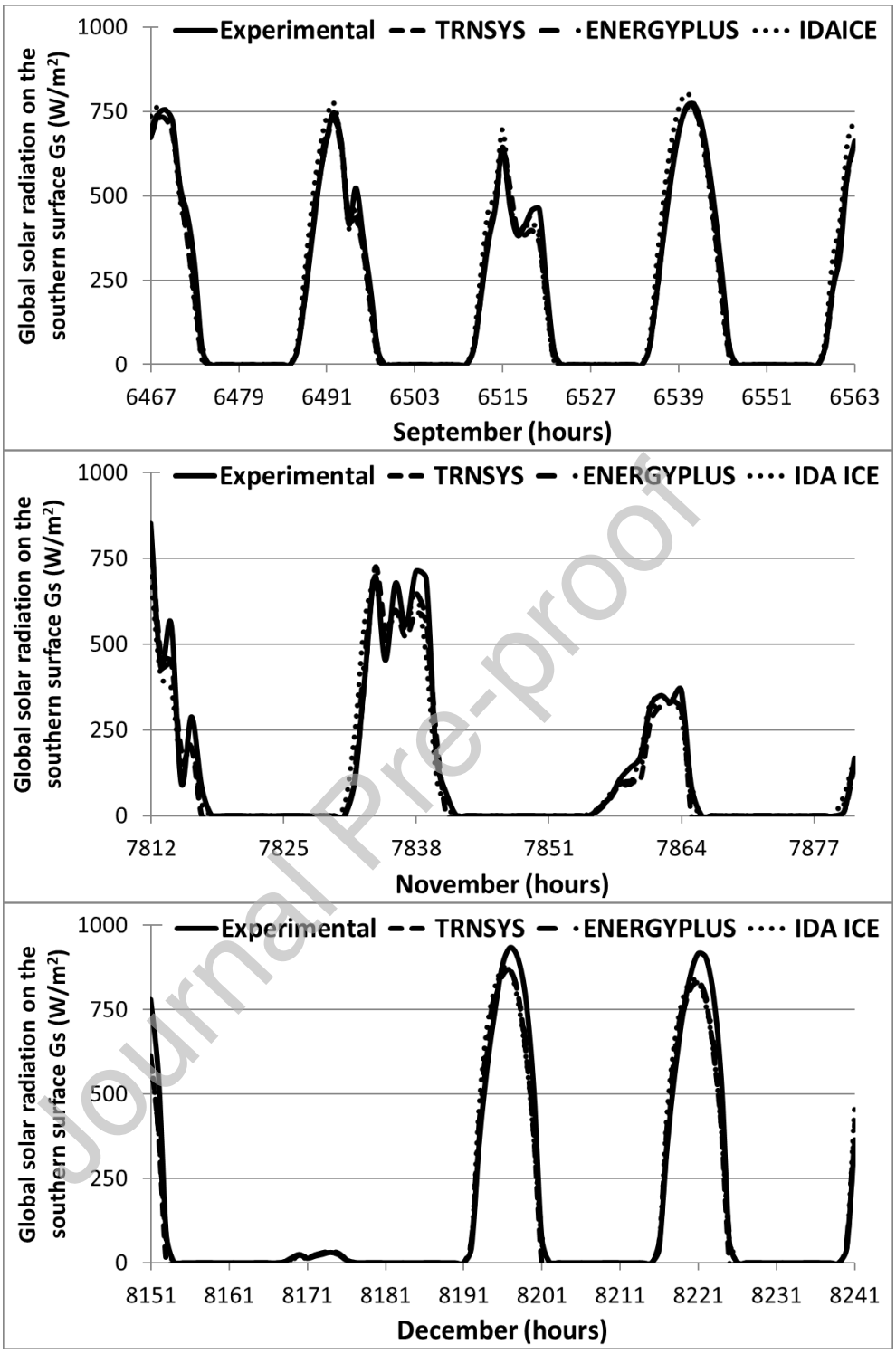

Figure 10 – Comparison of the experimental and simulated trends of the internal air temperature, and glass internal and external surface temperatures in September for the reference STB.

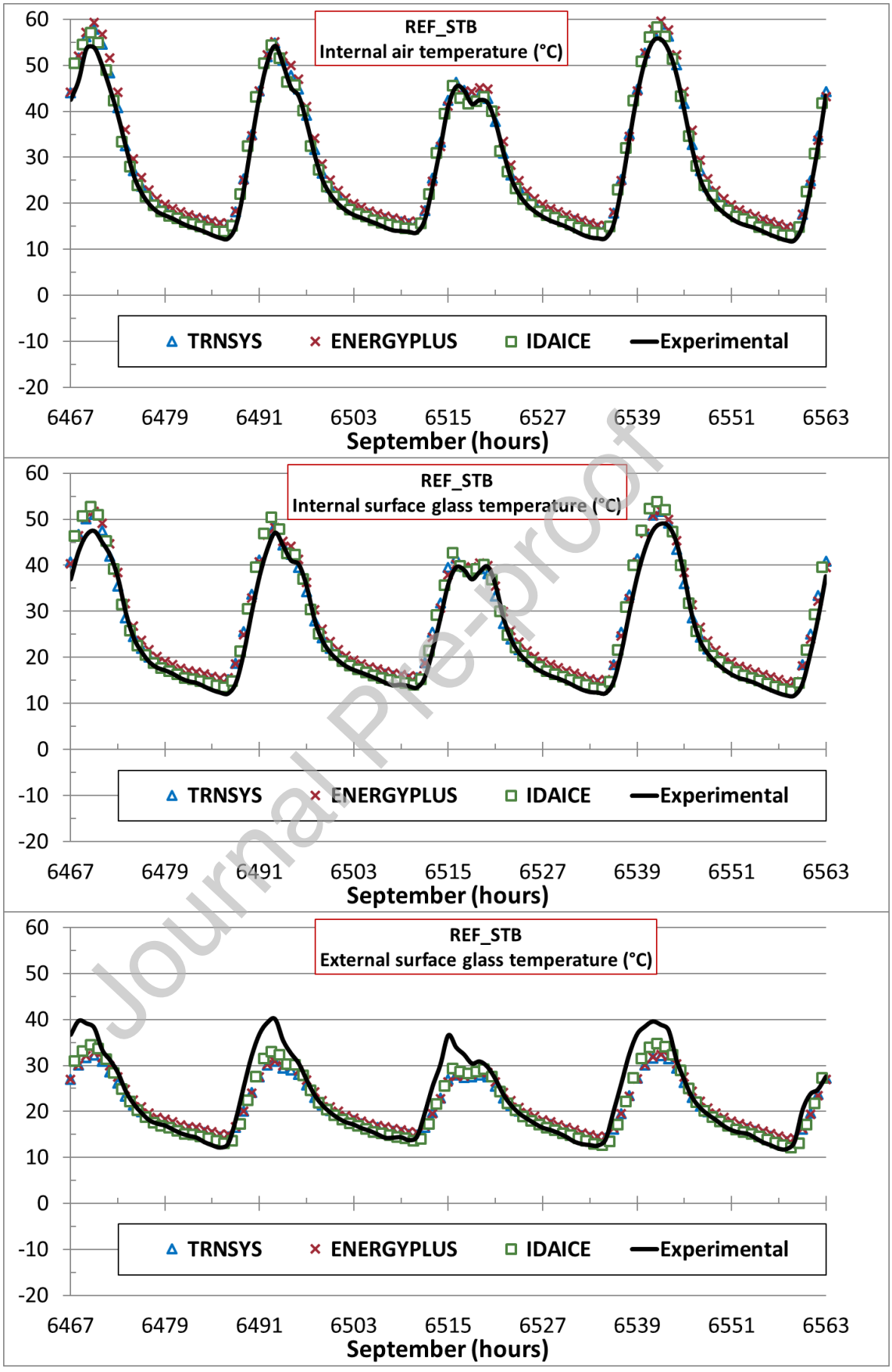

Figure 11 – Comparison of the experimental and simulated trends of the internal air temperature, and glass internal and external surface temperatures in November for the reference STB.

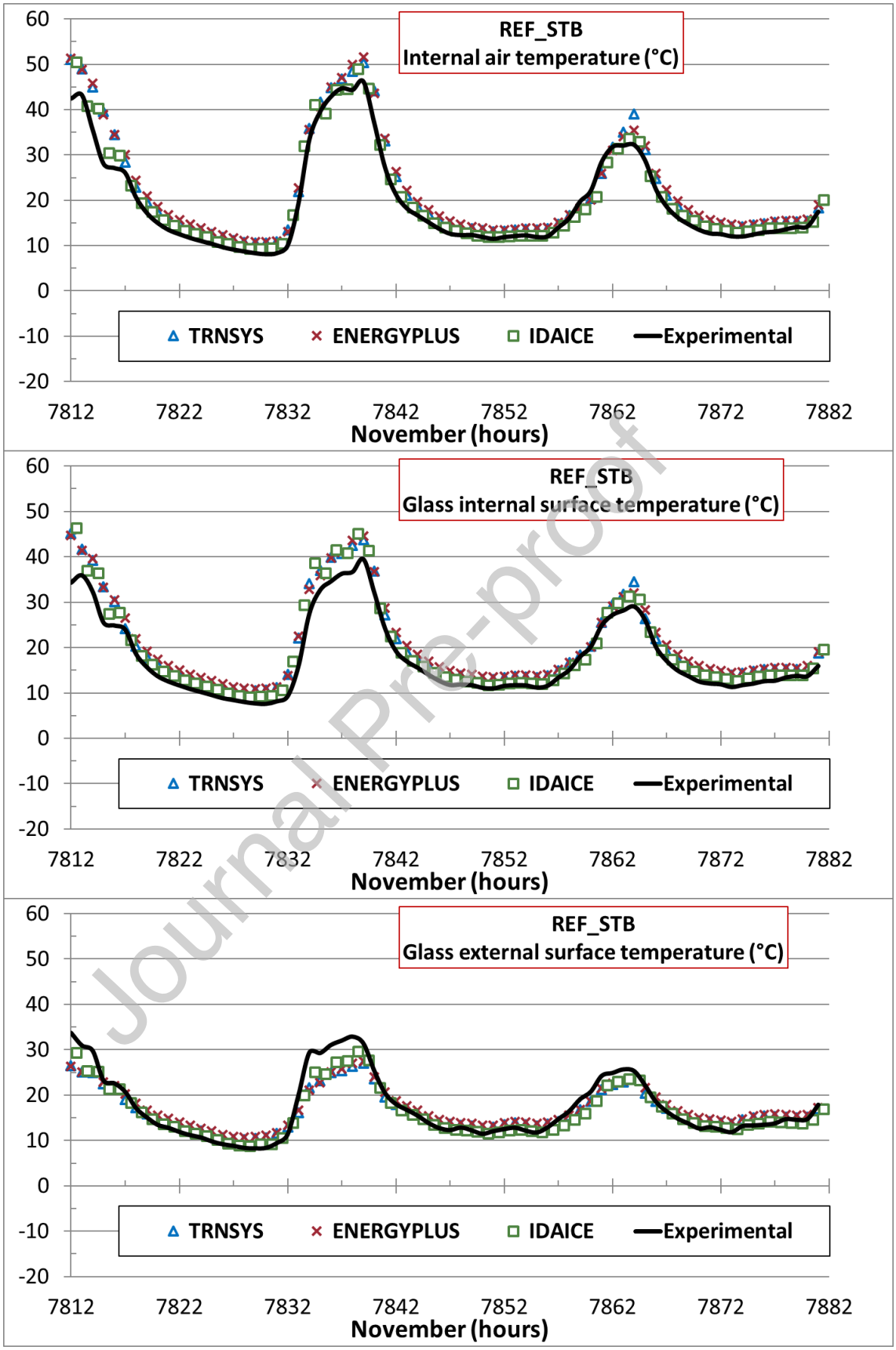

Figure 12 – Comparison of the experimental and simulated trends of the internal air temperature, and glass internal and external surface temperatures in December for the reference STB.

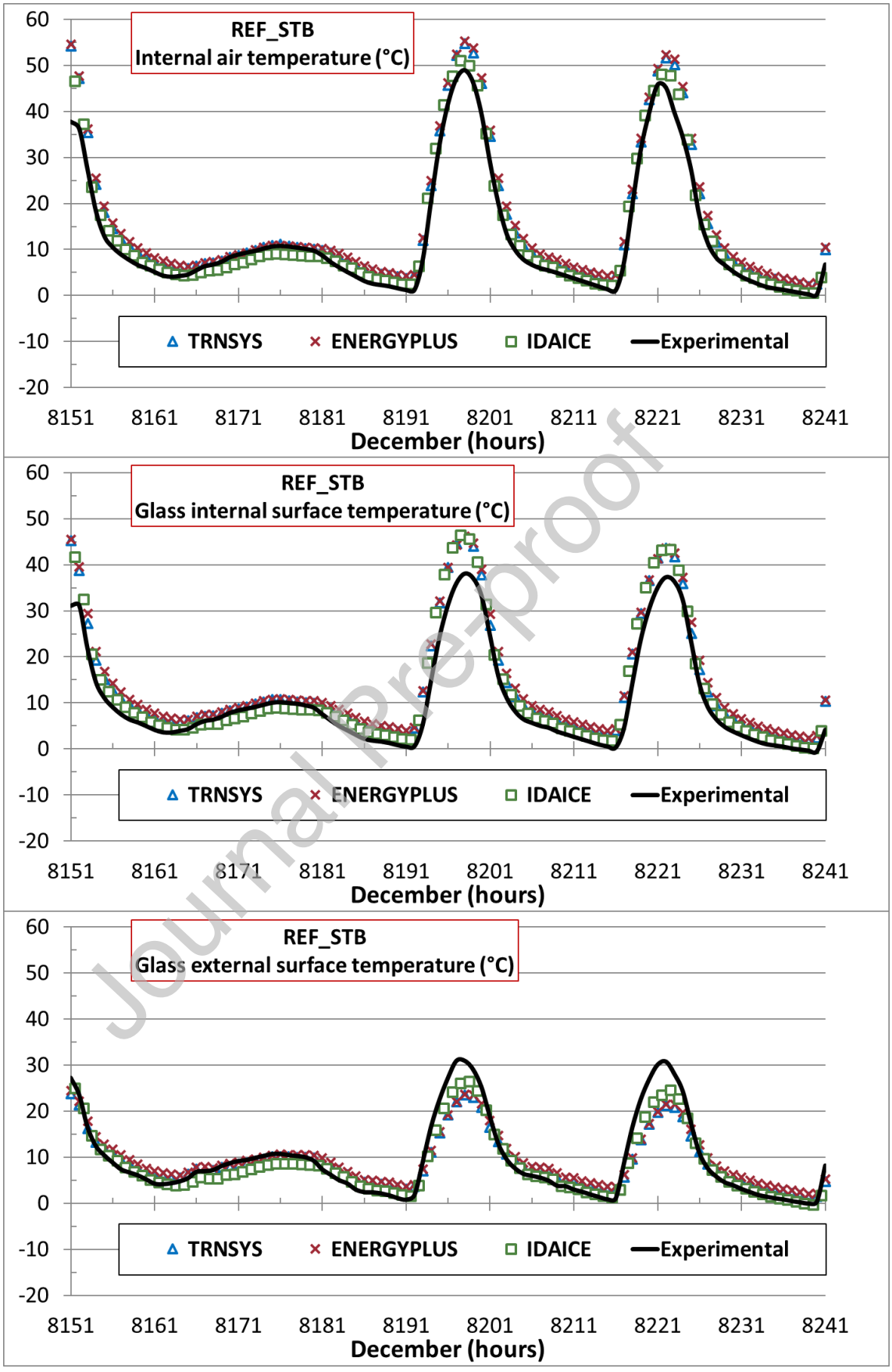

Figure 13 – Simulated internal air temperature trend for different air infiltration flow rates.

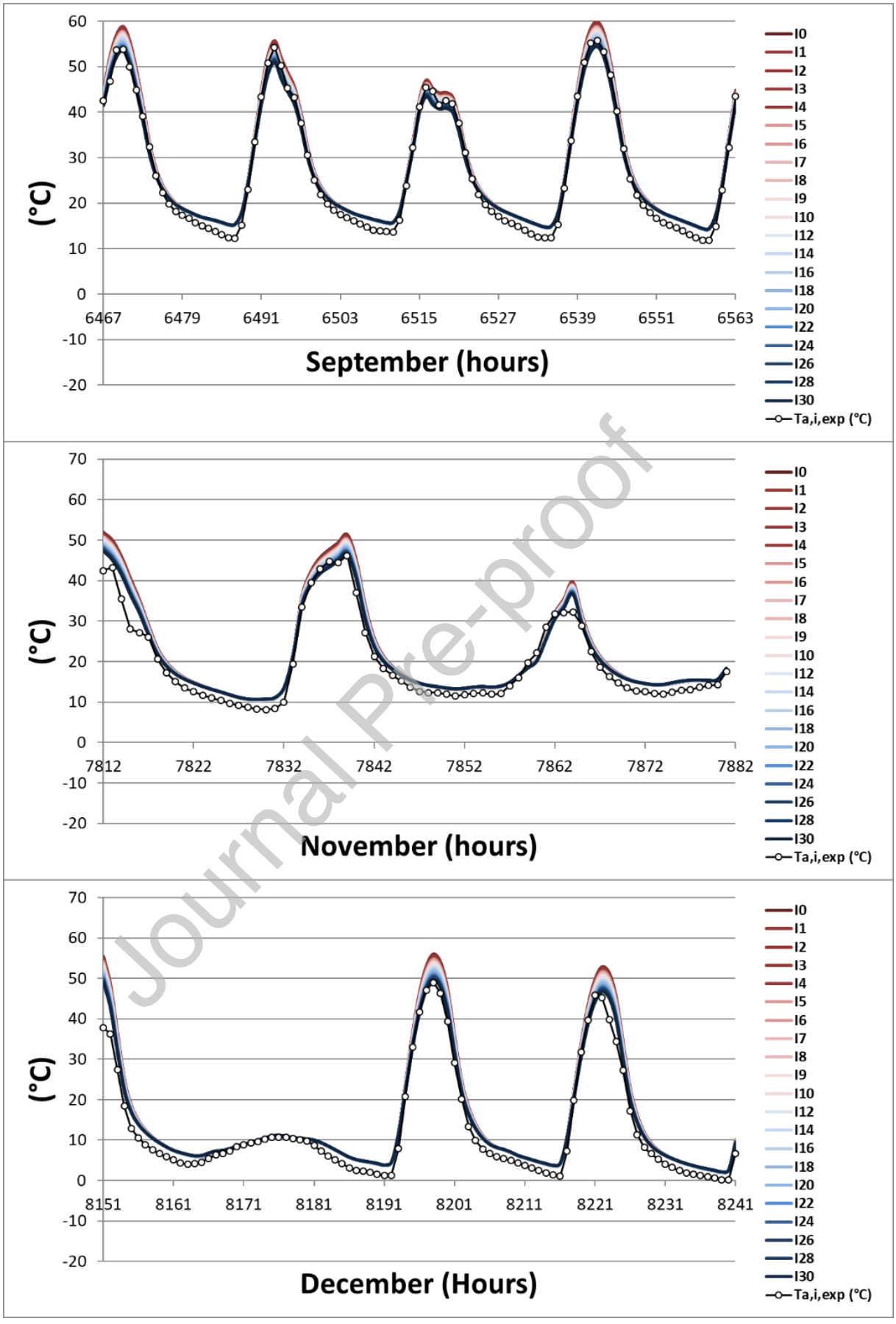

Figure 14 - Systematic error for each tool on the glass exterior surface temperature as a function of the incident global solar radiation on the southern wall by considering data of all the three periods considered.

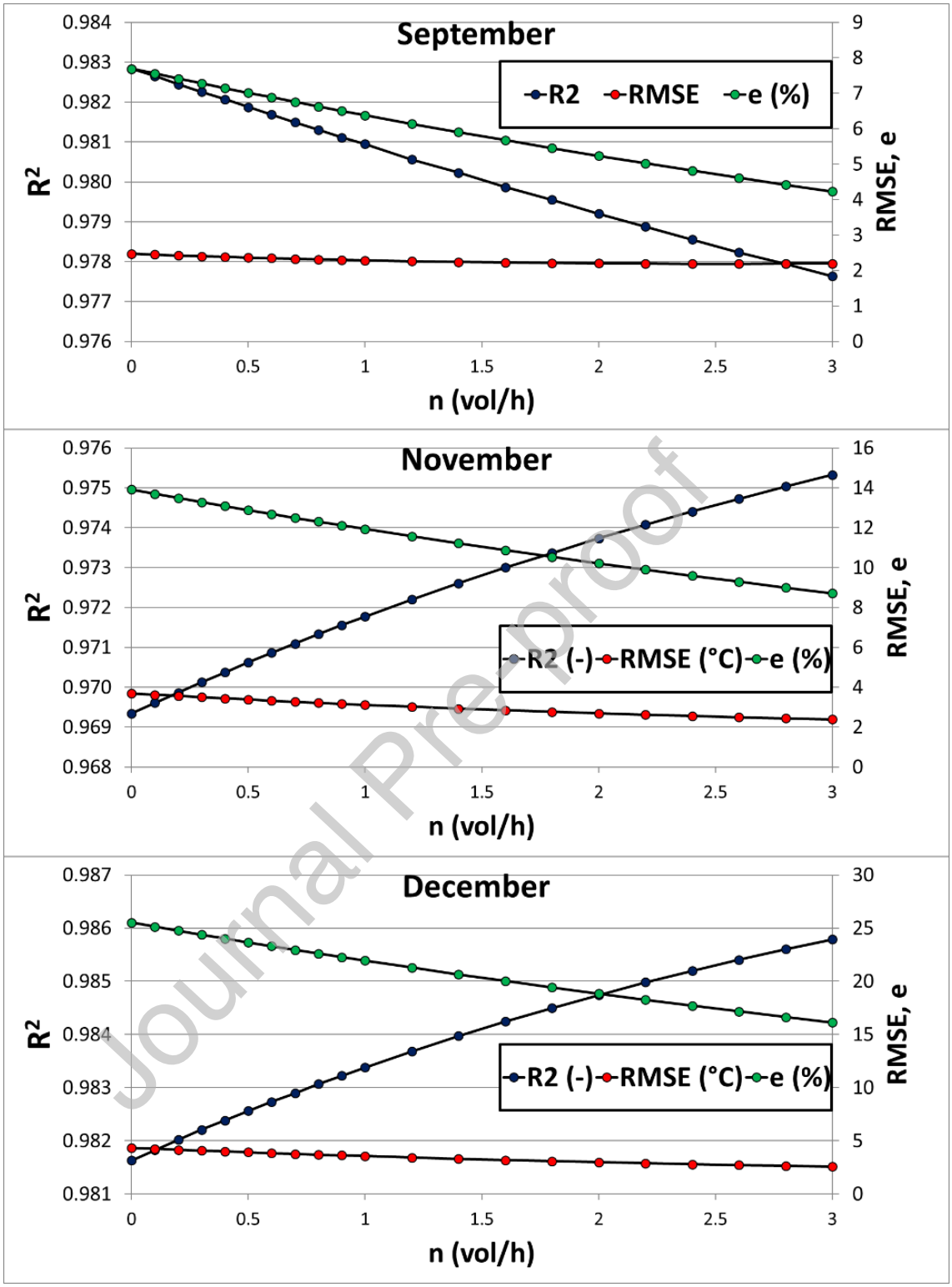

Figure 15 – Accuracy indices in September for the reference STB.

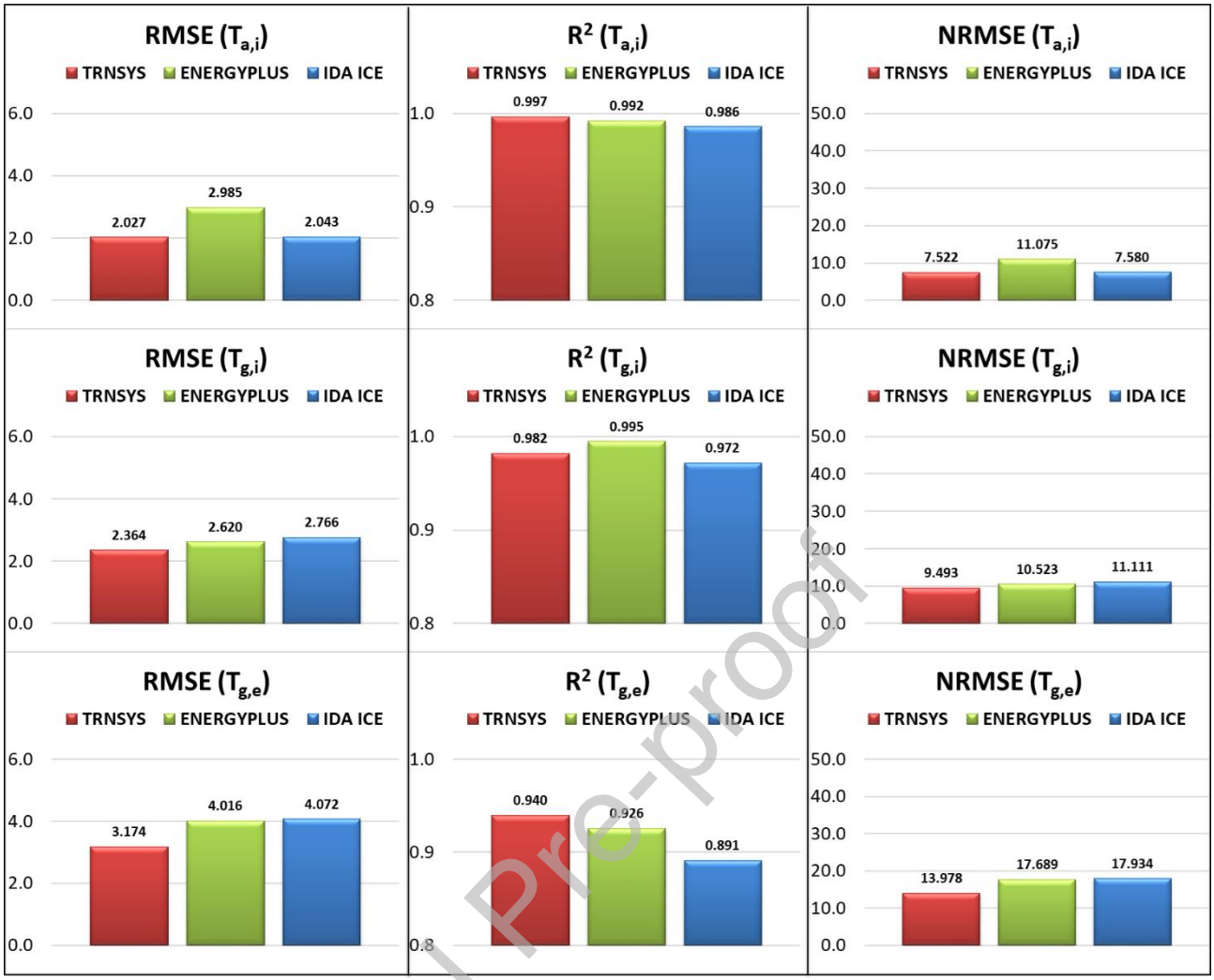

Figure 16 – Accuracy indices in November for the reference STB.

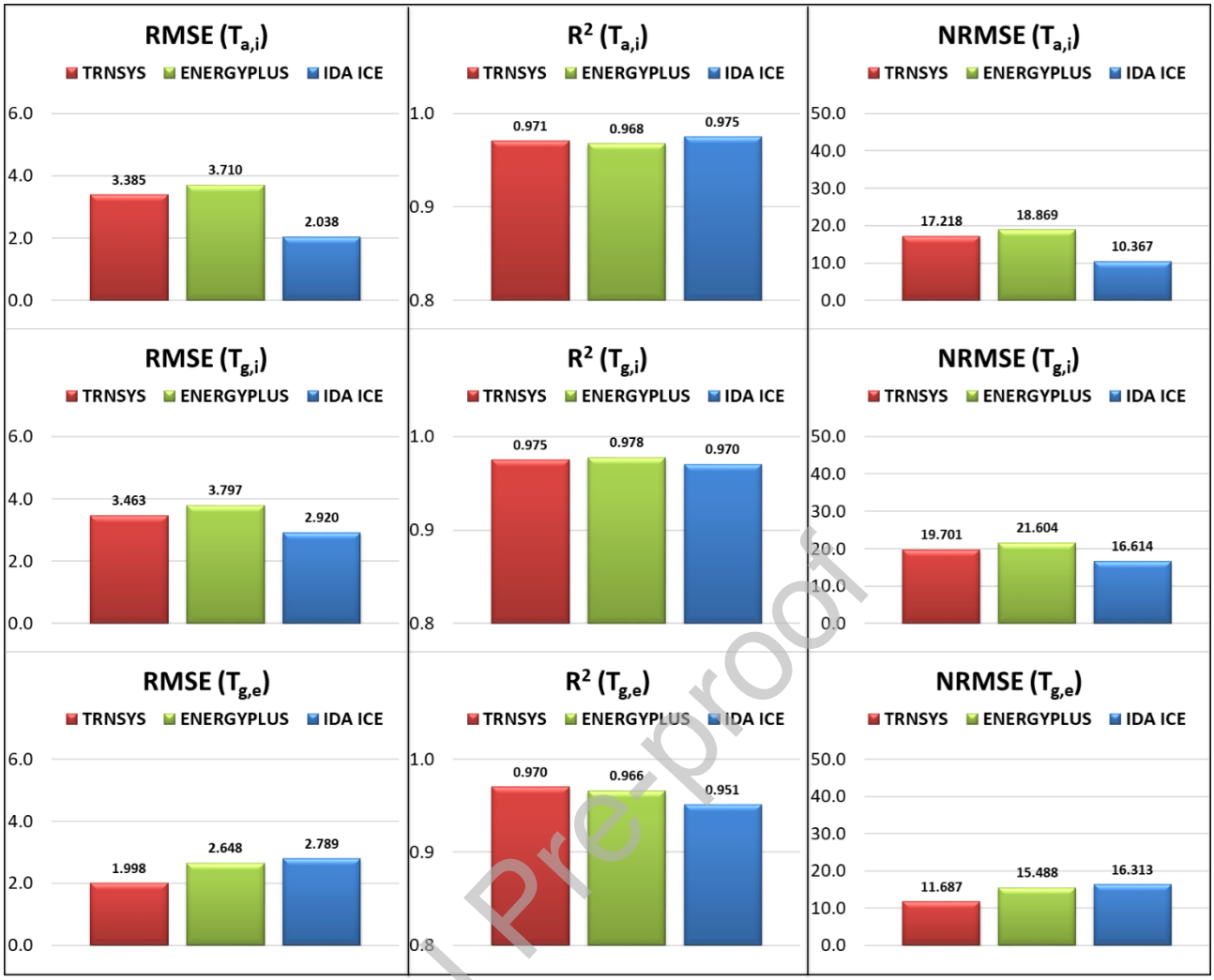

Figure 17 – Accuracy indices in December for the reference STB.

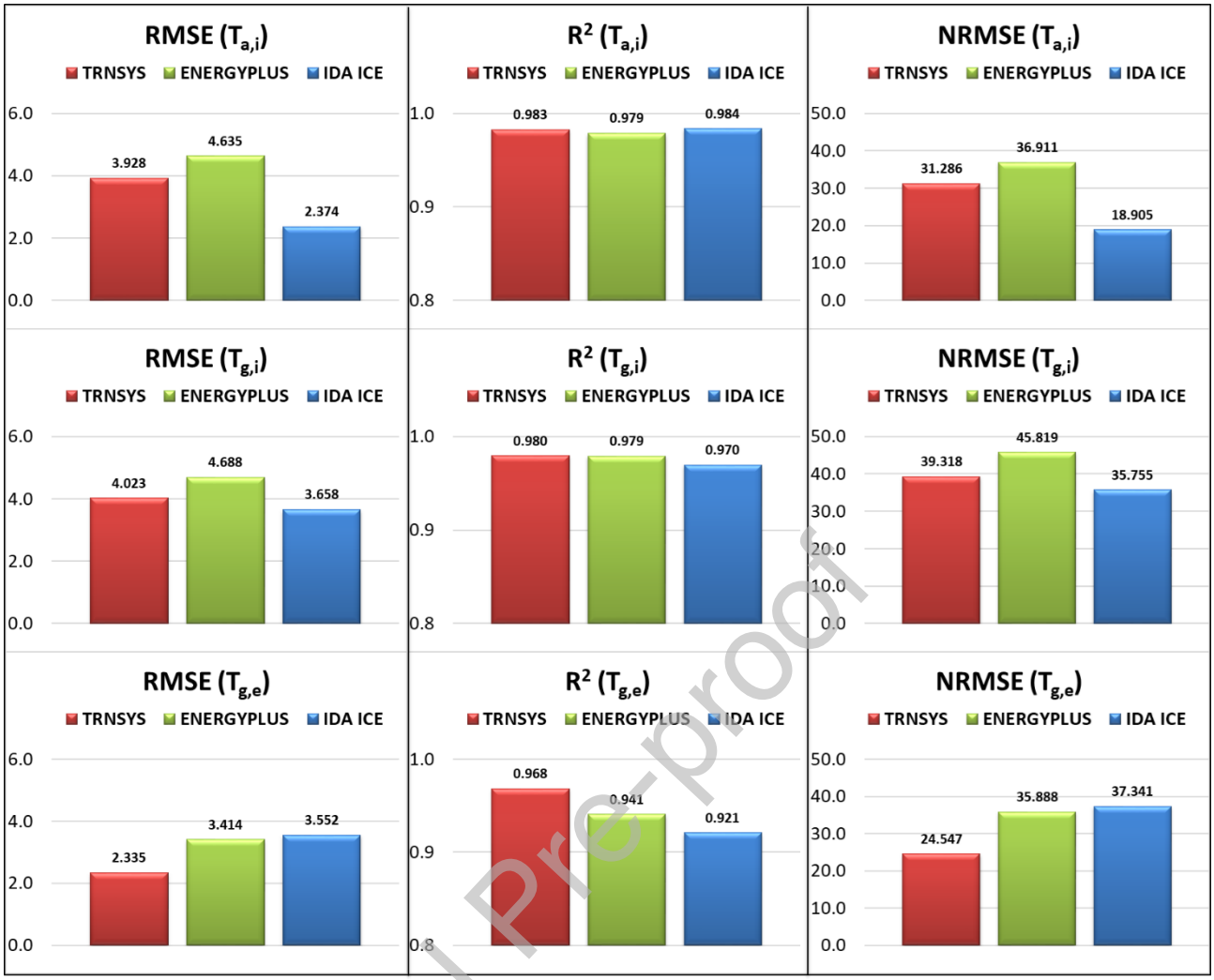

Figure 18 – Comparison of the experimental and simulated trends of the internal air temperature, glass internal and external surface temperatures, and PCM floor internal surface temperature in September for the PCM STB.

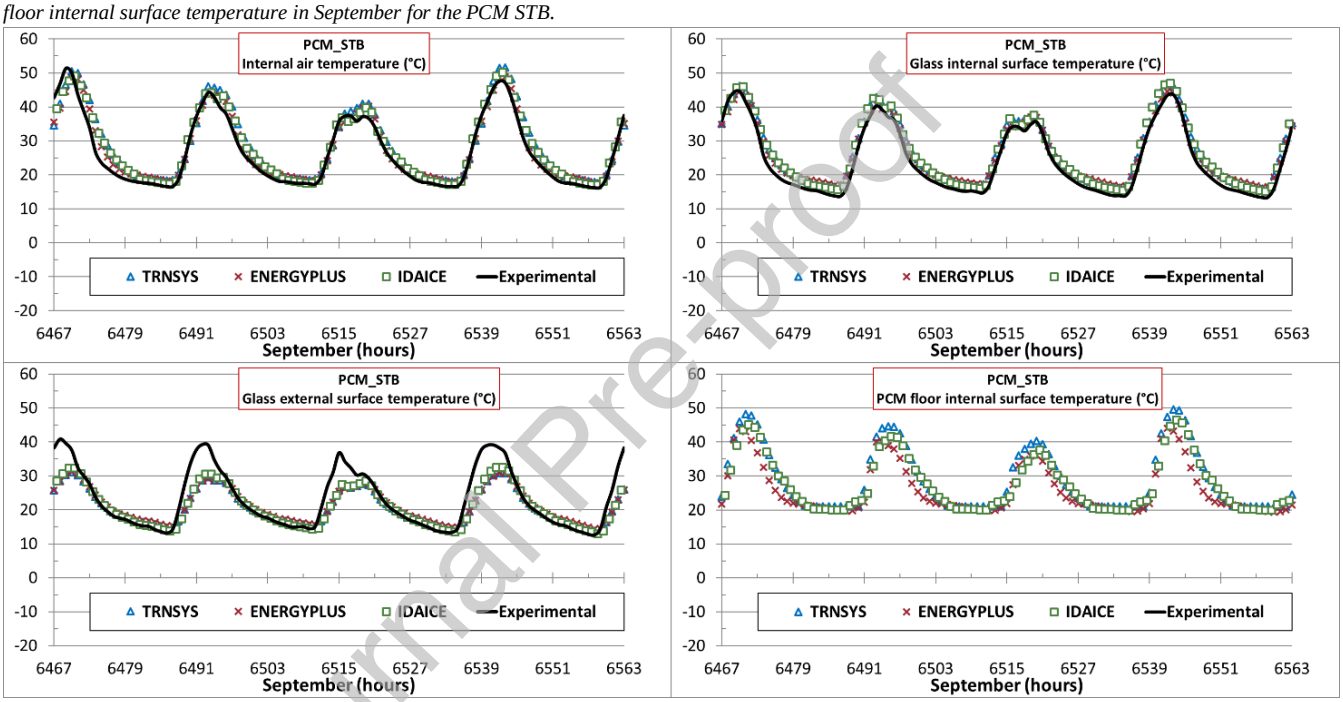

Figure 19 – Comparison of the experimental and simulated trends of the internal air temperature, glass internal and external surface temperatures, and PCM floor internal surface temperature in November for the PCM STB.

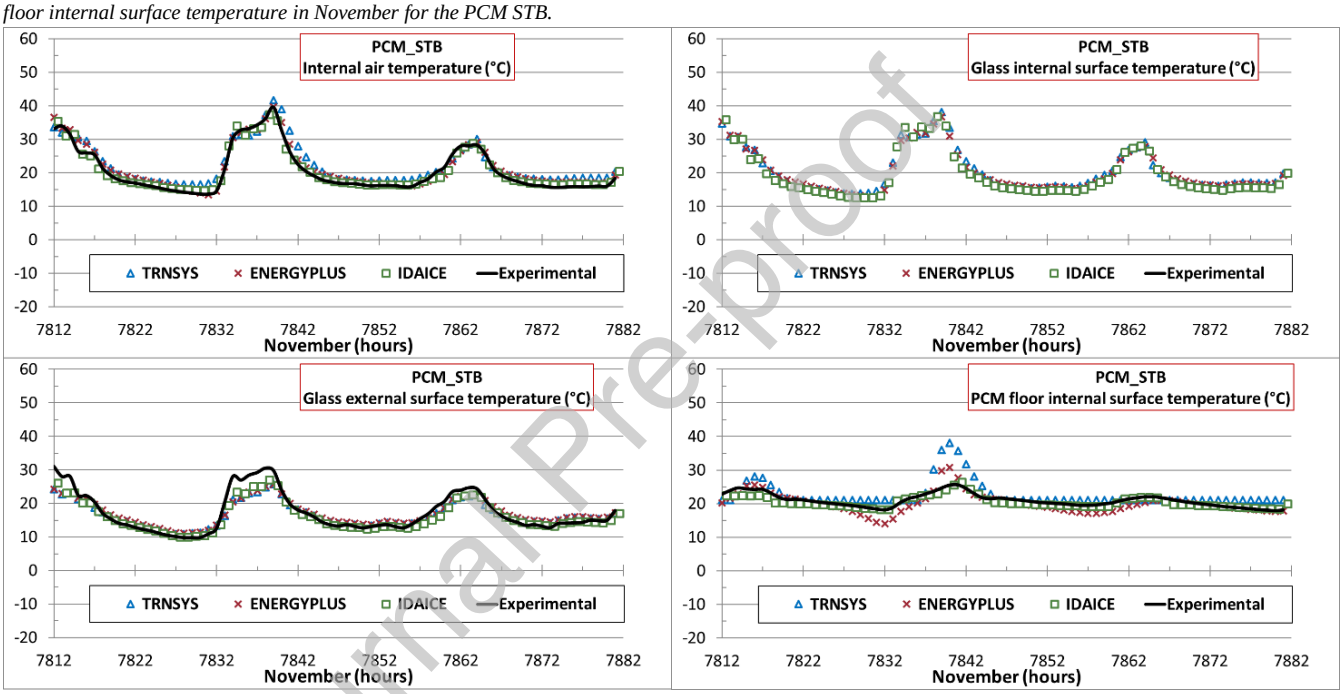

Figure 20 – Comparison of the experimental and simulated trends of the internal air temperature, glass internal and external surface temperatures, and PCM floor internal surface temperature in December for the PCM STB.

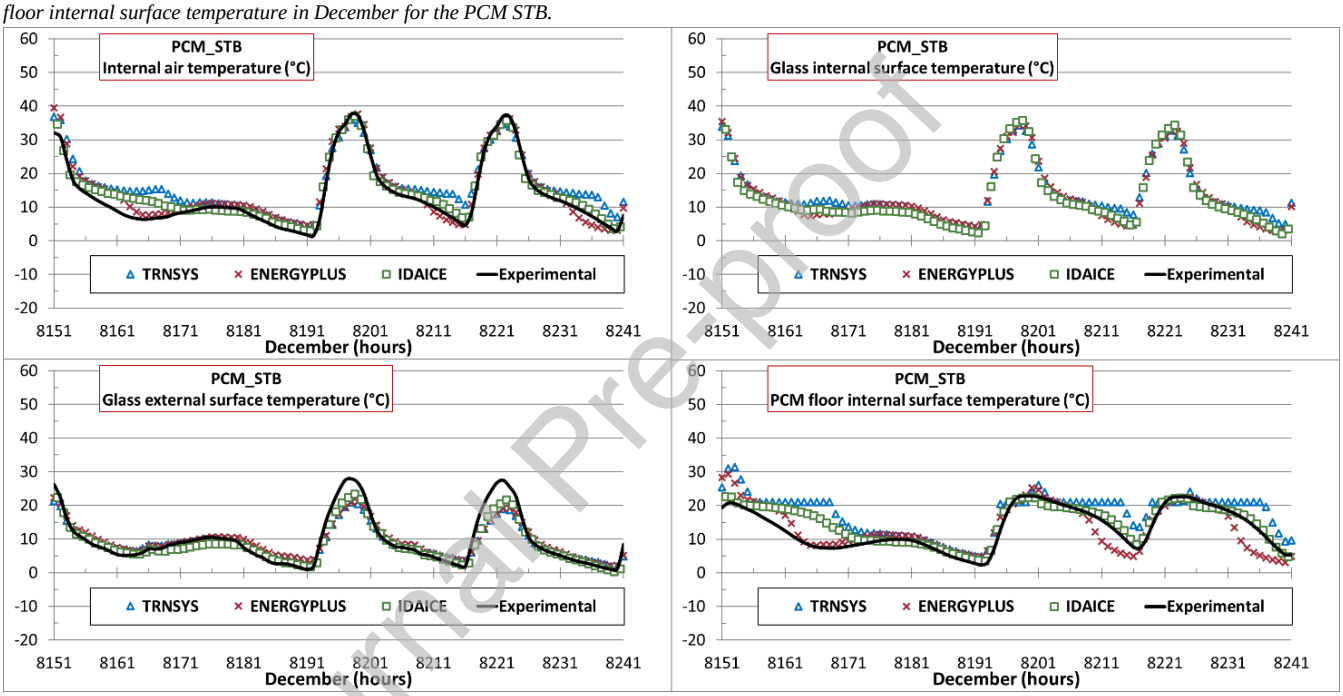

Figure 21 – Accuracy indices in September for the PCM STB.

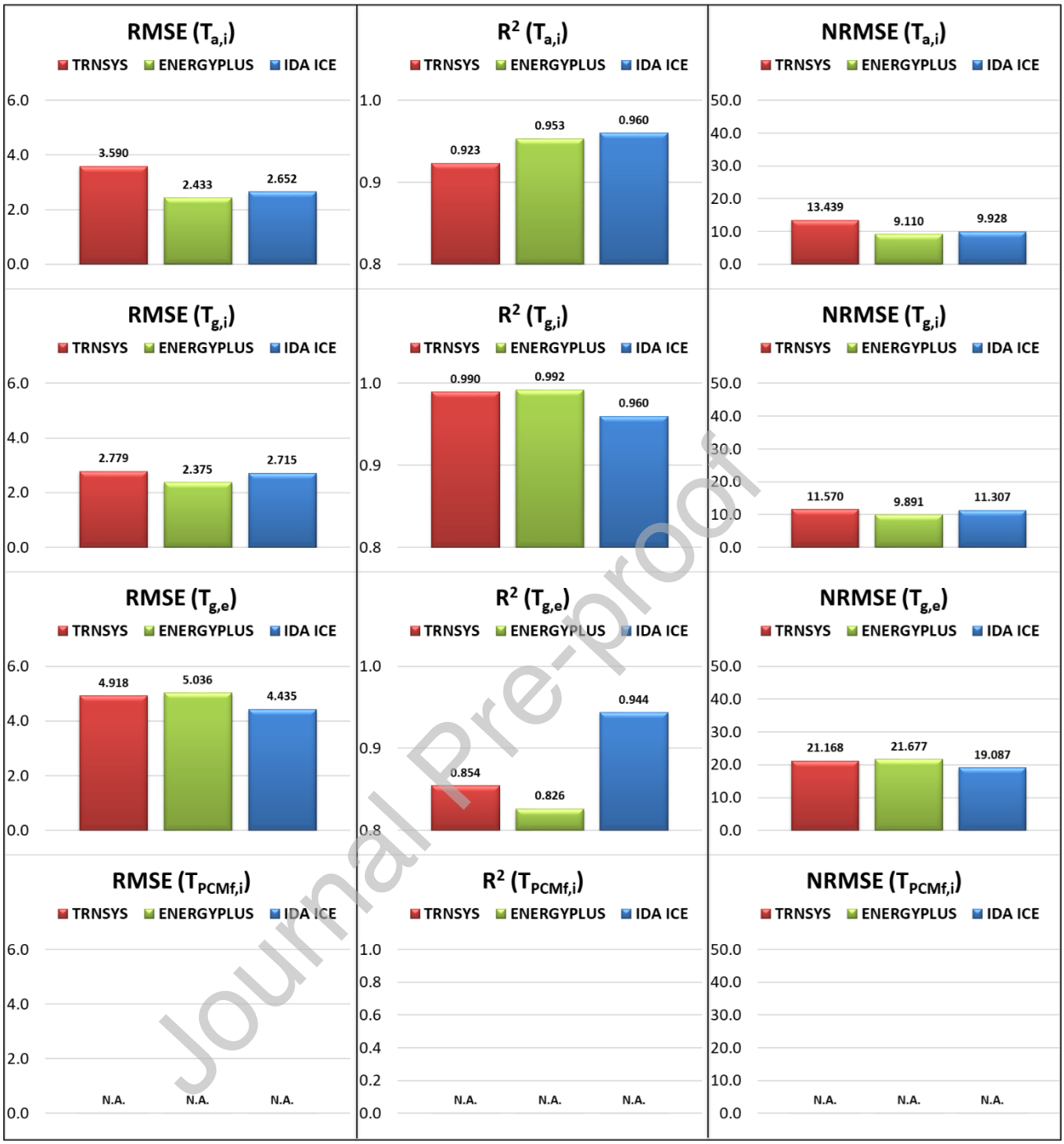

Figure 22 – Accuracy indices in November for the PCM STB.

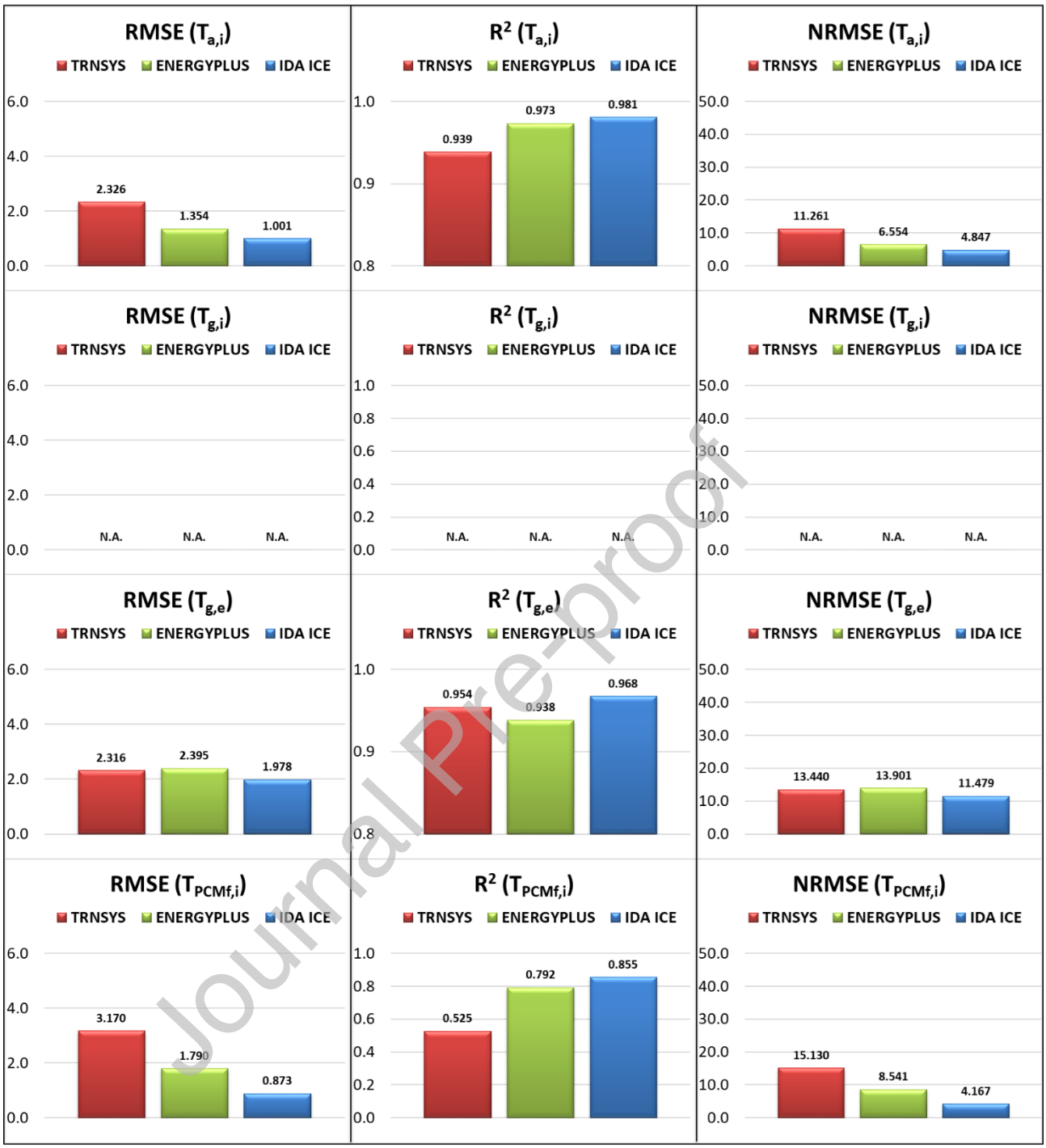

Figure 23 – Accuracy indices in December for the PCM STB.